



|              |  |
|--------------|--|
| Title        | Studies on Novel Environmentally Friendly Yellow and Orange Inorganic Pigments |
| Author(s)    | Bae, Byungseo  |
| Citation     | 大阪大学, 2018, 博士論文   |
| Version Type | VoR  |
| URL          | <a href="https://doi.org/10.18910/69552">https://doi.org/10.18910/69552</a>    |
| rights       |  |
| Note         |  |

*The University of Osaka Institutional Knowledge Archive : OUKA*

<https://ir.library.osaka-u.ac.jp/>

The University of Osaka

# **Studies on Novel Environmentally Friendly Yellow and Orange Inorganic Pigments**

(新規な環境調和型の黄色および橙色無機顔料に関する研究)

**Byungseo Bae**

**2018**

Division of Applied Chemistry  
Graduate School of Engineering,  
Osaka University

## *Preface*

The work of this thesis has been carried out under the supervision of Professor Dr. Nobuhito Imanaka at Department of Applied Chemistry, Graduate School of Engineering, Osaka University.

The object of this thesis is to develop novel environmentally friendly inorganic yellow and orange pigments and identify the color development mechanism.

The author wishes that the findings and the knowledge obtained in this work provide useful suggestions and information for further development and establishment of novel environmentally friendly inorganic pigments and that the materials would contribute to more practical applications.

A handwritten signature in black ink, appearing to be 'Byungseo Bae', written in a cursive style.

Byungseo Bae

Department of Applied Chemistry

Graduate School of Engineering

Osaka University

2-1 Yamadaoka, Suita,

Osaka 565-0871,

Japan

January 2018

# Contents

|  |   |
|--|---|
| <b><i>General Introduction</i></b> ..... | 1 |
|--|---|

|  |   |
|--|---|
| <b><i>List of Publications</i></b> ..... | 5 |
|--|---|

## ***Chapter 1***

### **Synthesis of Novel Inorganic Yellow Pigments using Rare Earth ions as a colorant (Eu<sup>2+</sup> and Ce<sup>3+</sup>)**

#### ***Chapter 1.1***

##### **Synthesis of Novel Inorganic Yellow Pigments Based on Gehlenite-type Structure (Ca<sub>2</sub>Al<sub>2</sub>SiO<sub>7</sub>)**

|         |   |       |    |
|---------|---|-------|----|
| 1.1.1   | Introduction  | ..... | 6  |
| 1.1.2   | Experimental Procedure  | ..... | 7  |
| 1.1.3   | Results and Discussion  | ..... | 8  |
| 1.1.3.1 | (Ca <sub>1-x</sub> Eu <sub>x</sub> ) <sub>2</sub> Al <sub>2</sub> SiO <sub>7+δ</sub> (0 ≤ x ≤ 0.15)                       | ..... | 8  |
| 1.1.3.2 | (Ca <sub>0.90-y</sub> Eu <sub>0.10</sub> Zn <sub>y</sub> ) <sub>2</sub> Al <sub>2</sub> SiO <sub>7+δ</sub> (0 ≤ y ≤ 0.05) | ..... | 11 |
| 1.1.4   | Conclusion  | ..... | 15 |

## **Chapter 1.2**

### **Novel Environmentally Friendly Yellow Pigments Based on Rare Earth Tungstate ( $\text{Ln}_2\text{W}_2\text{O}_9$ ; Ln = Pr, Sm, Gd)**

|         |  |       |    |
|---------|--|-------|----|
| 1.2.1   | Introduction   | ..... | 17 |
| 1.2.2   | Experimental Procedure   | ..... | 18 |
| 1.2.3   | Results and Discussion   | ..... | 19 |
| 1.2.3.1 | $(\text{Ln}_{1-x}\text{Ce}_x)_2\text{W}_2\text{O}_{9+\delta}$ (Ln = $\text{Pr}^{3+}$ , $\text{Sm}^{3+}$ , $\text{Gd}^{3+}$ ) | ..... | 19 |
| 1.2.3.2 | $(\text{Gd}_{1-x}\text{Ce}_x)_2\text{W}_2\text{O}_{9+\delta}$ ( $0 \leq x \leq 0.30$ )                                       | ..... | 21 |
| 1.2.3.3 | $(\text{Gd}_{0.80-y}\text{Ce}_{0.20}\text{Tb}_y)_2\text{W}_2\text{O}_{9+\delta}$ ( $0 \leq y \leq 0.03$ )                    | ..... | 26 |
| 1.2.4   | Conclusion   | ..... | 32 |

## **Chapter 2**

### **Synthesis of Novel Inorganic Orange Pigment using Transition Metal Ion as a colorant ( $\text{Ni}^{2+}$ )**

|     |                        |       |    |
|-----|------------------------|-------|----|
| 2.1 | Introduction           | ..... | 33 |
| 2.2 | Experimental Procedure | ..... | 34 |
| 2.3 | Results and Discussion | ..... | 35 |
| 2.4 | Conclusion             | ..... | 41 |

## ***Chapter 3***

### **Synthesis of Novel Inorganic Orange Pigment with anisotropic structure and their high NIR reflectivity**

|     |                                |       |    |
|-----|--------------------------------|-------|----|
| 3.1 | Introduction                   | ..... | 42 |
| 3.2 | Experimental Procedure         | ..... | 43 |
| 3.3 | Results and Discussion         | ..... | 44 |
| 3.4 | Conclusion                     | ..... | 51 |
|     | <b><i>Summary</i></b>          | ..... | 52 |
|     | <b><i>References</i></b>       | ..... | 54 |
|     | <b><i>Acknowledgements</i></b> | ..... | 58 |

## ***General Introduction***

The pigment, which originated from the Latin word “pigmentum”, was originally referred to a color for the coloring matter, but later the meaning is extended as colored decoration. Now, pigment means a material consisting of small particles with physically and chemically stable that are substantially insoluble, and used for coloring and protection by covering the substance with a dispersion media. The color of pigment is determined by selective visible light absorption, and yield from complementary color of absorbed visible light.

The use of natural inorganic pigments has been known. For example, over 30,000 years ago, the cave murals of Altamira in Spain and Apollo 11 Cave in Namibia were left and painted by using colored soil or rock like charcoal, manganese brown, clay, etc. Lead antimonate ( $\text{Pb}_3\text{Sb}_2\text{O}_8$ ), Egyptian blue ( $\text{CaCuSi}_4\text{O}_{10}$ ), and copper hydroxychloride ( $\text{Cu}_2(\text{OH})_3\text{Cl}$ ) were the first yellow, blue, and green pigment manufactured in history, respectively. Pigment technology has advanced through Egypt and Babylon civilization, and in the early Renaissance, blue glass containing safflower and cobalt was developed in Europe. The pigment industry has begun with Berlin Blue ( $\text{Fe}_4[\text{Fe}(\text{CN})_6]_3 \cdot x\text{H}_2\text{O}$ , 1704), Cobalt Blue ( $\text{CoAl}_2\text{O}_4$ , 1777), Scheele's green ( $\text{AsCuHO}_3$ , 1778) and Chrome Yellow ( $\text{PbCrO}_4$ ) in the 18th century [1]. In the 19<sup>th</sup> century, ultramarine ( $(\text{Na,Ca})_8(\text{AlSiO}_4)_6(\text{SO}_4,\text{S,Cl})_2$ ), Guignet's green ( $\text{Cr}_2\text{O}(\text{OH})_4$ ), cobalt pigments, iron oxide pigments, and cadmium pigments were developed [1]. Recently, mixed oxide, such as cadmium red ( $\text{Cd}(\text{S,Se})$ ), manganese blue ( $\text{BaMnO}_4 \cdot \text{BaSO}_4$ ), and molybdate red ( $25\text{PbCrO}_4 \cdot 4\text{PbMoO}_4 \cdot \text{PbSO}_4$ ), and new white synthetic pigments such as, titanium dioxide ( $\text{TiO}_2$ ) and zinc oxide ( $\text{ZnO}$ ), came into use in industry, and the importance of pigment is increasing [1].

Pigments are divided into organic pigments and inorganic pigments. All organic pigments are composed of carbon compounds (carbon and hydrogen). The organic pigments

extracted from natural sources have been used for centuries, but synthetic organic pigments derived from coal tars and other petrochemicals are mostly used today. Organic pigments show vivid and colorful colors, and have high tinting power. However, they can only be used for a relatively limited purpose because they lack heat resistance, light resistance against ultraviolet light, and durability to the surrounding environment. Inorganic pigments were obtained from rocks and clay in the past, but now the synthetic inorganic pigments are mostly used since the particle size of natural inorganic pigment has ununiformity and impurities. Synthetic inorganic pigments including oxide, nitride, and sulfide do not show vivid and colorful color compare to organic pigments, but they can be used for various applications due to their outstanding heat resistance, durability, wet-injury resistance and light resistance against ultraviolet light. Therefore, the important parts of inorganic pigments are paint, vanish, plastic, ink, construction materials, rubber, glasses and cosmetic.

The kind of color of inorganic pigment is decided by the colorant ions which absorbed light with a specific wavelength in the range of visible light. The nature of these colorant ions depends on the peripheral electrons, and therefore, transition metals having a partially filled *d* sub-shell are generally applied. The color of the materials containing transition metal can be controlled because the valence and the coordination number of the transition metal is easily changed by changing the peripheral electrons created by a covalent bond or ionic bond, etc [2]. The colorant ions for inorganic pigment can be divided into; 1). Ions that always provide a color (V, Cr, Mn, Fe, Ni, Co, Cu, U, etc.), 2). Ions that provide a color under certain conditions (Ti, Cd, Sb, Bi, etc.), 3). Ions that do not always provide a color (Li, Na, K, Mg, Ca, Sr, Ba, B, Si, Al, etc.) [3]. Therefore, inorganic pigments with vivid color, such as chrome yellow ( $\text{PbCrO}_4$ ), cadmium zinc yellow ( $\text{CdS-ZnS}$ ), titanate yellow ( $\text{TiO}_2\text{-NiO-Sb}_2\text{O}_3$ ), lead red ( $2\text{PbO-PbO}_2$ ), cadmium selenide red ( $\text{CdSe-CdS}$ ), mercuric sulfide red ( $\text{HgS}$ ), and cobalt aluminate blue ( $\text{CoAl}_2\text{O}_4$ ), have been synthesized and used. However, these inorganic pigments contain toxic

elements (Pb, Cr, Cd, Sb, Se, Hg and Co) which are dangerous not only to human body but also to the environment. Therefore, the use of these elements is severely circumscribed for tougher sanctions [4, 5] such as RoHS (Restriction of Hazardous Substances) Directive [6]. In addition, some sulfides and oxynitrides, such as  $\text{Ce}_2\text{S}_3$ ,  $\text{La}_2\text{S}_3$ ,  $\text{Ce}_4\text{Si}_3\text{S}_{12}$  [7, 8],  $\text{Sm}_{14}\text{W}_4\text{O}_{33-3x}\text{N}_{2x}$  and  $\text{Ca}_{(1-x)}\text{La}_x\text{TaO}_{(2-x)}\text{N}_{(1+x)}$  [9, 10], were also tried to be synthesized as the inorganic pigments due to their vivid color, although conventional inorganic pigments are mostly oxide compounds. Mixing other pigments with sulfide sometimes causes changes in color due to their relatively low chemical stability. Most of sulfides react with acid to generate hydrogen sulfide, and they oxidize to sulfate or oxide by heating in atmospheric condition. Oxynitrides require the toxic and flammable ammonia gas in their synthesis [9, 10]. In the case of incineration of waste sulfides and oxynitrides,  $\text{NO}_x$  or  $\text{SO}_x$  gas which is harmful to human body and environment is discharged. Therefore, oxides are emerging as the most powerful candidate from the environmental and economic points of view.

Now, environmentally friendly inorganic oxide pigments such as praseodymium yellow ( $\text{ZrSiO}_4:\text{Pr}$ ), iron oxide red ( $\text{Fe}_2\text{O}_3$ ) and bayferrox orange ( $\text{Fe}_2\text{O}_3\text{-FeO(OH)}$ ) are widely used, but chromaticity of them were less as compared to inorganic pigments containing toxic element. Furthermore, iron oxide red ( $\text{Fe}_2\text{O}_3$ ) and bayferrox orange ( $\text{Fe}_2\text{O}_3\text{-FeO(OH)}$ ) are weak against high temperature and UV light. Therefore, many research groups are trying to develop new environmentally friendly inorganic pigments [11-34]. Imanaka research group is one of them [34-44], and so far, several inorganic pigments which meet the environmental regulations have been successfully synthesized. But still, the chromaticity is not enough similarly to the above cases.

In order to develop new environmentally friendly inorganic pigments, it is essential to select harmless elements as the base materials and the color activator. In this doctoral research, novel environmentally friendly inorganic pigments are synthesized along with the above plan.

In addition to the previously used transition metal ions in the colorant, rare-earth ions whose atom have partially filled  $d$  sub-shell, which have not been used in the past, are also used to synthesize pigments and the color properties are investigated.

This thesis consists of the following three chapters.

**In Chapter 1,**

1) Synthesis of novel environmentally friendly inorganic yellow pigments,  $(\text{Ca}_{1-x-y}\text{Eu}_x\text{Zn}_y)_2\text{Al}_2\text{SiO}_{7+\delta}$  ( $0 \leq x \leq 0.15$ ;  $0 \leq y \leq 0.07$ ) solids with gehlenite-type structure, is described. Also it is shown that the proportion of  $\text{Eu}^{2+}$  as a colorant was increased by doping  $\text{Zn}^{2+}$  ion into the  $\text{Ca}_2\text{Al}_2\text{SiO}_7$  lattice, and the yellowness was increased as compared with  $(\text{Ca}_{0.90}\text{Eu}_{0.10})_2\text{Al}_2\text{SiO}_{7+\delta}$  pigment.

2) The novel environmentally friendly inorganic yellow pigments,  $(\text{Ln}_{1-x}\text{Ce}_x)_2\text{W}_2\text{O}_{9+\delta}$  ( $\text{Ln} = \text{Pr}^{3+}$ ,  $\text{Sm}^{3+}$ , and  $\text{Gd}^{3+}$ ) with monoclinic structure, are described. Furthermore, since the  $(\text{Gd}_{1-x}\text{Ce}_x)_2\text{W}_2\text{O}_{9+\delta}$  solids showed the brilliant yellowness among the prepared pigments,  $\text{Tb}^{3+}$  ion was doped into the  $(\text{Gd}_{0.80}\text{Ce}_{0.20})_2\text{W}_2\text{O}_{9+\delta}$  lattice to further increase the yellowness of  $(\text{Gd}_{1-x}\text{Ce}_x)_2\text{W}_2\text{O}_{9+\delta}$  solids by controlling the crystal field of  $\text{Ce}^{3+}$  ion.

In **Chapter 2**, the novel environmentally friendly inorganic orange pigments,  $\text{Ba}(\text{Ni}_{1-x}\text{Mn}_x)_2\text{P}_2\text{O}_7$  ( $0 \leq x \leq 0.30$ ) solids with monoclinic structure, are described. The crystal field and concentration of  $\text{Ni}^{2+}$  ions were controlled by doping  $\text{Mn}^{2+}$  ions into the  $\text{BaNiP}_2\text{O}_7$  lattice, and the redness was successfully increased.

In **Chapter 3**, the novel environmentally friendly inorganic orange pigments,  $\text{Sr}_4\text{Mn}_2(\text{Cu}_{1-x}\text{Zn}_x)\text{O}_9$  ( $0 \leq x \leq 1$ ) solids with hexagonal perovskite-type structure, are described. By controlling the anisotropic lattice distortion by doping  $\text{Zn}^{2+}$  ions into the  $\text{Sr}_4\text{Mn}_2\text{CuO}_9$  lattice, the redness of the pigment increased.

## List of Publications

1. Novel Environmentally Friendly Inorganic Yellow Pigments Based on Gehlenite-type Structure  
**Byungseo Bae**, Wendusu, Shinji Tamura, and Nobuhito Imanaka,  
*Ceram. Int.*, 42 (2016) 15104~15106.
2. Novel Environment-Friendly Yellow Pigments Based on Praseodymium (III) Tungstate  
**Byungseo Bae**, Shinji Tamura, and Nobuhito Imanaka,  
*Ceram. Int.*, 43 (2017) 7366~7368.
3. Novel Environment-Friendly Orange Pigments Based on Hexagonal Perovskite 2H and Their High NIR Reflectivity  
**Byungseo Bae**, Shinji Tamura, and Nobuhito Imanaka,  
*Dyes Pigm.*, 147 (2017) 523~528.
4. Novel Environmentally Friendly Yellow Pigments Based on Rare Earth Tungstate ( $\text{Ln}_2\text{W}_2\text{O}_9$ ; Ln = Pr, Sm, Gd)  
**Byungseo Bae**, Shinji Tamura, and Nobuhito Imanaka,  
in preparation.
5. Novel Environmentally Friendly Orange Pigments Based on  $\text{BaNiP}_2\text{O}_7$   
**Byungseo Bae**, Shinji Tamura, and Nobuhito Imanaka,  
in preparation.

## ***Chapter 1***

### **Synthesis of Novel Inorganic Yellow Pigments using Rare Earth ions as a colorant (Eu<sup>2+</sup> and Ce<sup>3+</sup>)**

#### ***Chapter 1.1***

### **Synthesis of Novel Inorganic Yellow Pigments Based on Gehlenite-type Structure (Ca<sub>2</sub>Al<sub>2</sub>SiO<sub>7</sub>)**

#### **1.1.1 Introduction**

Novel environmentally friendly yellow pigment using rare earth ion as a colorant was synthesized based on calcium aluminum silicate (gehlenite: Ca<sub>2</sub>Al<sub>2</sub>SiO<sub>7</sub>). Gehlenite itself shows white color but suitable as a base material for environmentally friendly pigment because it consists of harmless and abundant elements. In order to produce yellow color, Eu<sup>2+</sup> ion is used as a colorant. Eu<sup>2+</sup> ion has 4f<sup>7</sup>-4f<sup>6</sup>5d transition which may allow absorption in wide visible light region. The color of this pigment, especially yellowness, depends on the position of absorption edge, which can be controlled by two parameters, concentration and crystal field around Eu<sup>2+</sup> ion. Therefore, it is expected that this pigment shows vivid yellowness.

In order to develop inorganic yellow pigment, Ca<sup>2+</sup> ions in Ca<sub>2</sub>Al<sub>2</sub>SiO<sub>7</sub> lattice were partially substituted with Eu<sup>2+</sup> ion. Namely, (Ca<sub>1-x</sub>Eu<sub>x</sub>)<sub>2</sub>Al<sub>2</sub>SiO<sub>7+δ</sub> samples were synthesized, and the preparation condition and composition were optimized. As mentioned above, in order to increase the proportion of Eu<sup>2+</sup> ion in the (Ca<sub>0.90</sub>Eu<sub>0.10</sub>)<sub>2</sub>Al<sub>2</sub>SiO<sub>7+δ</sub> pigment, Zn<sup>2+</sup> ion was doped into Ca<sub>2</sub>Al<sub>2</sub>SiO<sub>7</sub> lattice to release local strain caused by ionic size mismatch. As a result,

novel  $(\text{Ca}_{1-x-y}\text{Eu}_x\text{Zn}_y)_2\text{Al}_2\text{SiO}_{7+\delta}$  ( $0 \leq x \leq 0.15$ ;  $0 \leq y \leq 0.05$ ) inorganic yellow pigments are described because  $4f^7-4f^65d$  transition of  $\text{Eu}^{2+}$  ion is the origin of yellow color. The color properties of pigments were studied in relation to the doping effect of  $\text{Zn}^{2+}$ .

### 1.1.2 Experimental Procedure

The  $(\text{Ca}_{1-x-y}\text{Eu}_x\text{Zn}_y)_2\text{Al}_2\text{SiO}_{7+\delta}$  ( $0 \leq x \leq 0.15$ ;  $0 \leq y \leq 0.05$ ) samples were synthesized by the conventional solid state reaction method. Stoichiometric amounts of  $\text{CaCO}_3$ ,  $\text{Eu}_2\text{O}_3$ ,  $\text{ZnO}$ ,  $\text{Al}_2\text{O}_3$  and  $\text{SiO}_2$  powders were mixed in an agate mortar. Then, mechanical mixing was carried out with a planetary ball milling apparatus (Pulverisette 7 premium line, FRITSCHE GmbH) at a rotation speed of 300 rpm for 3 h. The homogeneous mixture was calcined at 900 °C for 10 hours under atmospheric air for decarbonation. After decarbonation, the obtained sample was reground in an agate mortar and sintered at 1350 °C for 6 h in a flow of 2% $\text{H}_2$ -98%Ar mixture gas.

The prepared samples were characterized by X-ray powder diffraction (XRD; Rigaku, SmartLab) with Cu-K $\alpha$  radiation (40 kV and 30 mA) to identify the crystal structure. The lattice volumes were calculated from the peak angles in the XRD patterns, which were refined using  $\alpha$ - $\text{Al}_2\text{O}_3$  as reference. X-ray fluorescence spectroscopy (XRF; Rigaku, ZSX-100e) measurements were conducted to confirm the composition of the samples. X-ray photoelectron spectroscopy (XPS; PHI5000 VersaProbe II, ULVAC-PHI) was measured at room temperature using Al-K $\alpha$  radiation (1486.6 eV). The charging effect on the binding energies was revised with respect to the C 1S peak at 284.6 eV. The optical reflectance spectrum measurement was measured with a UV-Vis spectrometer (Shimadzu, UV-2600) using barium sulfate as standard. The color properties of the samples were estimated in terms of CIE  $L^*a^*b^*$  system with a colorimeter (CR-400, Konica-Minolta). The parameter  $L^*$  represents the brightness or darkness in a neutral grey scale, and the parameters  $a^*$  (the red-green axis) and  $b^*$  (the yellow-blue axis)

indicate the color, respectively. Chroma parameter ( $C$ ) indicating the color saturation of a pigment was calculated by formula ( $C = [(a^*)^2 + (b^*)^2]^{1/2}$ ). Hue angle ( $H^\circ$ ) which ranges from 0 to  $360^\circ$  was calculated according to the following equation,  $H^\circ = \tan^{-1}(b^*/a^*)$ ;  $H^\circ = 90^\circ$  for pure yellow color.

### 1.1.3 Results and Discussion

#### 1.1.3.1 $(\text{Ca}_{1-x}\text{Eu}_x)_2\text{Al}_2\text{SiO}_{7+\delta}$ ( $0 \leq x \leq 0.15$ ) pigments

**Figure 1.1.1** shows the XRD patterns of the  $(\text{Ca}_{1-x}\text{Eu}_x)_2\text{Al}_2\text{SiO}_{7+\delta}$  ( $0 \leq x \leq 0.15$ ) samples. A single gehlenite phase was obtained for the samples in the range of  $0 \leq x \leq 0.10$ , and there were no extra peaks of other compounds or impurity phases. However, for samples with  $x = 0.12$ , a  $\text{Ca}_2\text{SiO}_4$  phase was observed as impurity in addition to the gehlenite phase.

The lattice volume of the  $(\text{Ca}_{1-x}\text{Eu}_x)_2\text{Al}_2\text{SiO}_{7+\delta}$  ( $0 \leq x \leq 0.12$ ) samples depicts in **Figure 1.1.2**. The lattice volume of the gehlenite phase increased with increasing Eu ion content in the range of  $0 \leq x \leq 0.10$ , while the gehlenite lattice volume was almost constant in the range of  $x > 0.1$ . It means that Ca ion was replaced with Eu ions, and formed the solid solution for the samples with  $x \leq 0.1$ . Excess Eu ion could not successfully be substituted in gehlenite lattice causing Ca-based impurity to formed and lattice volume to be constant for samples of  $x > 0.1$ , thus the solubility limit of Eu ion in gehlenite lattice is  $x = 0.1$ .

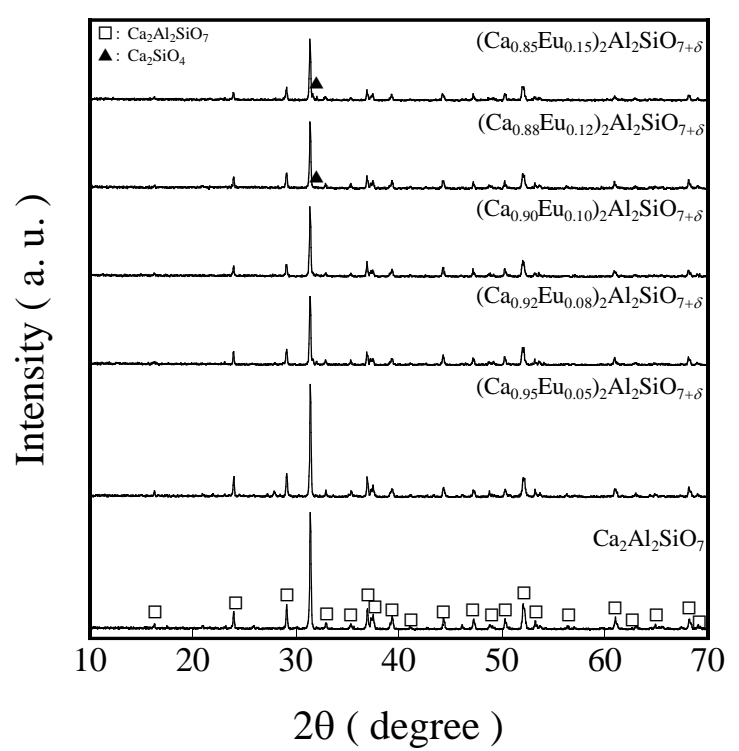


**Figure 1.1.1** XRD patterns of the  $(\text{Ca}_{1-x}\text{Eu}_x)_2\text{Al}_2\text{SiO}_{7+\delta}$  ( $0 \leq x \leq 0.15$ ) samples.

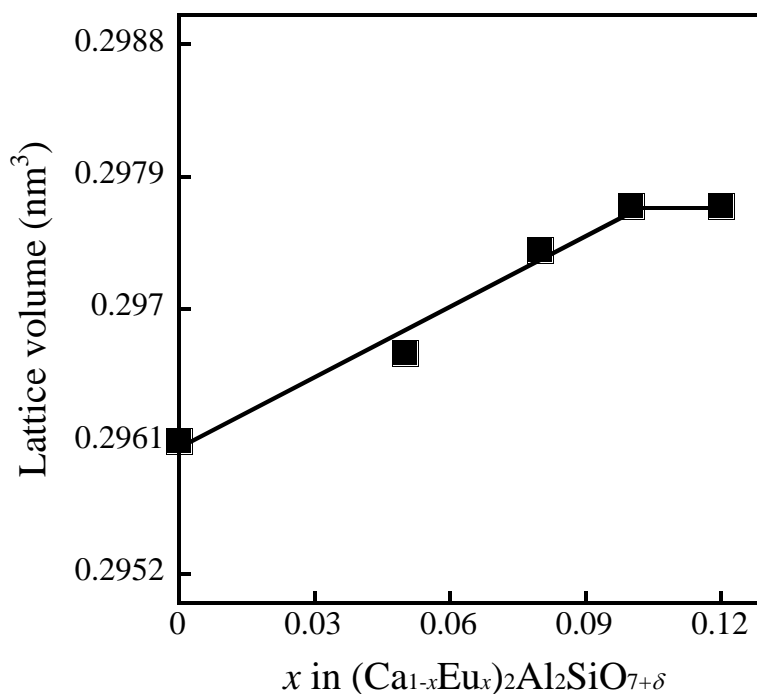


**Figure 1.1.2** Change in lattice volume as a function of  $x$  for the  $(\text{Ca}_{1-x}\text{Eu}_x)_2\text{Al}_2\text{SiO}_{7+\delta}$  ( $0 \leq x \leq 0.12$ ) samples.

**Figure 1.1.3** depicts the UV-vis diffuse reflectance spectra for the  $(\text{Ca}_{1-x}\text{Eu}_x)_2\text{Al}_2\text{SiO}_{7+\delta}$  ( $0 \leq x \leq 0.12$ ) samples. The  $\text{Ca}_2\text{Al}_2\text{SiO}_7$  sample exhibited high reflectance in visible light region. After  $\text{Eu}^{2+}$  ion doping, a strong optical absorption in the visible light region including the blue light region (435 – 480 nm) was observed, and the absorption edge shifted to longer wavelength direction of around 500 nm. Strong optical absorption is originated from  $4f^7-4f^65d$  transition of  $\text{Eu}^{2+}$  ion [45-47], and  $(\text{Ca}_{0.90}\text{Eu}_{0.10})_2\text{Al}_2\text{SiO}_{7+\delta}$  pigment showed the highest optical absorption in the blue light region among the prepared samples.

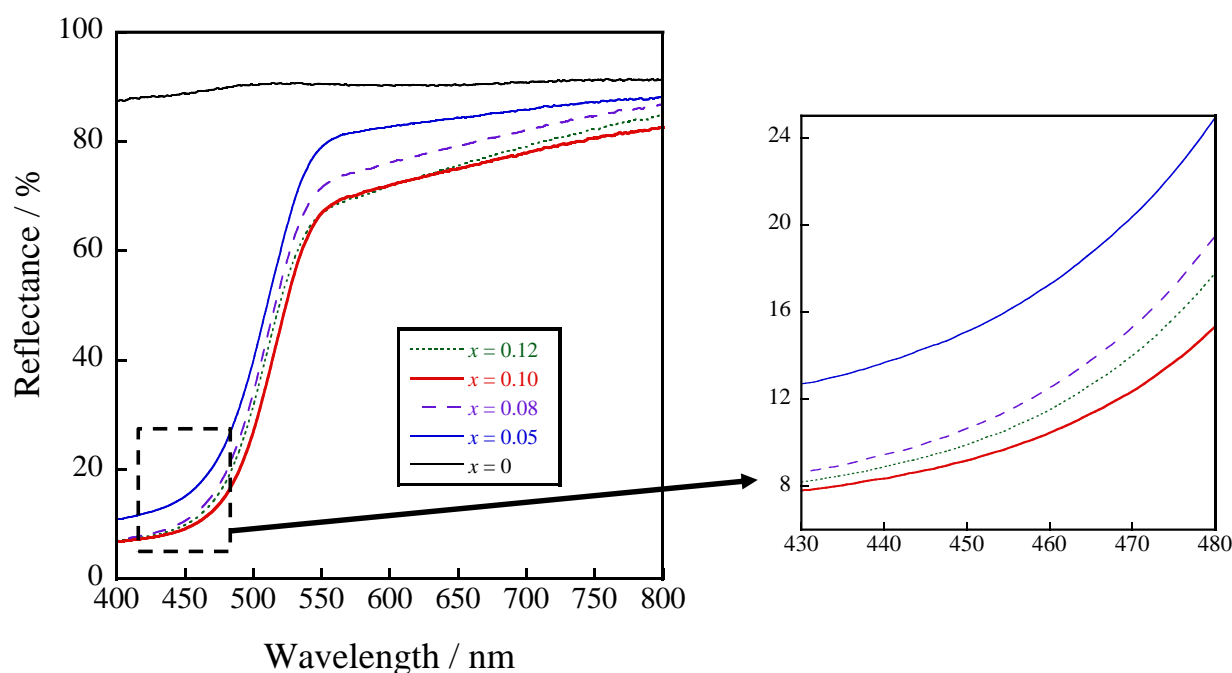


**Figure 1.1.3** UV-Vis diffuse reflectance spectra for the  $(\text{Ca}_{1-x}\text{Eu}_x)_2\text{Al}_2\text{SiO}_{7+\delta}$  ( $0 \leq x \leq 0.12$ ) samples.

**Table 1.1.1** tabulates the color parameters of the  $(\text{Ca}_{1-x}\text{Eu}_x)_2\text{Al}_2\text{SiO}_{7+\delta}$  ( $0 \leq x \leq 0.12$ ) samples. The yellow chromaticity ( $b^*$ ) and the color saturation parameter ( $C$ ) increased with

increasing concentration of Eu ion in the range of single-phase region of  $0 \leq x \leq 0.10$ , and the  $(\text{Ca}_{0.90}\text{Eu}_{0.10})_2\text{Al}_2\text{SiO}_{7+\delta}$  pigment showed the highest  $b^*$  and  $C$  values at +70.5 and 70.6 among the prepared samples, respectively. Decrease of the  $b^*$  and  $C$  values for the samples with  $x = 0.12$  are due to the influence of impurity  $\text{Ca}_2\text{SiO}_4$  phase, as seen in **Figure 1.1.1**.

**Table 1.1.1** CIE  $L^*a^*b^*CH^\circ$  color parameters for the  $(\text{Ca}_{1-x}\text{Eu}_x)_2\text{Al}_2\text{SiO}_{7+\delta}$  ( $0 \leq x \leq 0.12$ ) samples

| Samples  | $L^*$ | $a^*$ | $b^*$ | $C$  | $H^\circ$ |
|--|-------|-------|-------|------|-----------|
| $\text{Ca}_2\text{Al}_2\text{SiO}_7$                                   | 97.4  | -0.3  | +0.9  | 0.9  | 108.4°    |
| $(\text{Ca}_{0.95}\text{Eu}_{0.05})_2\text{Al}_2\text{SiO}_{7+\delta}$ | 87.5  | -7.0  | +63.9 | 64.3 | 96.3°     |
| $(\text{Ca}_{0.92}\text{Eu}_{0.08})_2\text{Al}_2\text{SiO}_{7+\delta}$ | 83.6  | -6.1  | +68.5 | 68.8 | 95.1°     |
| $(\text{Ca}_{0.90}\text{Eu}_{0.10})_2\text{Al}_2\text{SiO}_{7+\delta}$ | 83.0  | -4.2  | +70.5 | 70.6 | 93.4°     |
| $(\text{Ca}_{0.88}\text{Eu}_{0.12})_2\text{Al}_2\text{SiO}_{7+\delta}$ | 86.2  | -6.3  | +66.2 | 66.5 | 95.4°     |

### 1.1.3.2 $(\text{Ca}_{0.90-y}\text{Eu}_{0.10}\text{Zn}_y)_2\text{Al}_2\text{SiO}_{7+\delta}$ ( $0 \leq y \leq 0.05$ )

As mentioned in the previous section, the  $(\text{Ca}_{0.90}\text{Eu}_{0.10})_2\text{Al}_2\text{SiO}_{7+\delta}$  pigment exhibited the highest yellow hue. By increasing the proportion of  $\text{Eu}^{2+}$  ion in the pigment, the enhancement of yellow hue can be expected, because the origin of yellow color is the  $4f^7-4f^65d$  transition of divalent Eu ion. Therefore, in order to further increase the proportion of  $\text{Eu}^{2+}$  ion in the lattice,  $\text{Zn}^{2+}$  ion was additionally doped into the  $\text{Ca}^{2+}$  site in the  $(\text{Ca}_{0.90}\text{Eu}_{0.10})_2\text{Al}_2\text{SiO}_{7+\delta}$  pigment because  $\text{Zn}^{2+}$  ion has smaller ionic radius (0.09 nm for 8 coordination [50]) compared to that of  $\text{Ca}^{2+}$  ion (0.112 nm for 8 coordination [50]) and the difference in ionic radius (0.022 nm) between  $\text{Ca}^{2+}$  and  $\text{Zn}^{2+}$  is similar to that (0.018 nm) between  $\text{Eu}^{2+}$  (0.125 nm for 8 coordination [50]) and  $\text{Eu}^{3+}$  (0.1066 nm for 8 coordination [50]). Therefore, by the partial substitution of  $\text{Zn}^{2+}$  ion for  $\text{Ca}^{2+}$  ion, the proportion of  $\text{Eu}^{2+}$  ion, which has larger ionic radius

than  $\text{Eu}^{3+}$  ion, in the solid may increase due to relieve of crystal lattice strain generated by the doping of smaller  $\text{Zn}^{2+}$  ions into  $\text{Ca}^{2+}$  site.

**Figure 1.1.4** shows the XRD patterns of the  $(\text{Ca}_{0.90-y}\text{Eu}_{0.10}\text{Zn}_y)_2\text{Al}_2\text{SiO}_{7+\delta}$  ( $0 \leq y \leq 0.05$ ) pigments. A single phase of gehlenite-type structure was obtained for all samples, and there were no diffraction peaks of any impurities in the patterns.

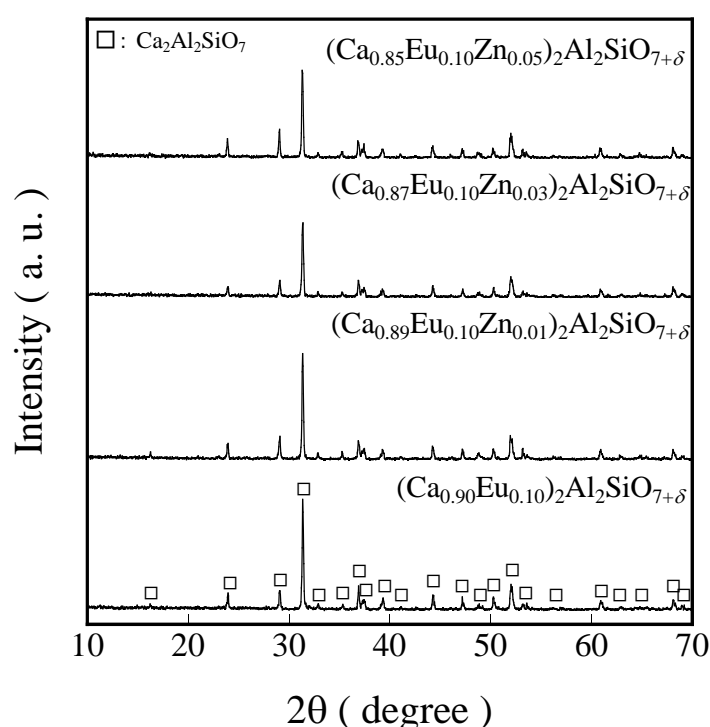


**Figure 1.1.4** XRD patterns of the  $(\text{Ca}_{0.90-y}\text{Eu}_{0.10}\text{Zn}_y)_2\text{Al}_2\text{SiO}_{7+\delta}$  ( $0 \leq y \leq 0.05$ ) pigments.

**Figure 1.1.5** illustrates the UV-visible diffuse reflectance spectra for the  $(\text{Ca}_{0.90-y}\text{Eu}_{0.10}\text{Zn}_y)_2\text{Al}_2\text{SiO}_{7+\delta}$  ( $0 \leq y \leq 0.05$ ) pigments. As same as the case in the previous section, a strong optical absorption in the visible light region including the blue light (435 – 480 nm), which was originated by the  $4f^7-4f^65d$  transition of  $\text{Eu}^{2+}$  [45-47], was observed for all

samples. The absorption edge shifted to longer wavelength direction with increasing  $Zn^{2+}$  ion concentration, and the optical absorption in the blue light region for  $(Ca_{0.87}Eu_{0.10}Zn_{0.03})_2Al_2SiO_{7+\delta}$  pigment was the most effectively enhanced. As mentioned above, to release the local strain for the crystal stabilization caused by ionic size mismatch between  $Ca^{2+}$  and  $Zn^{2+}$ , a portion of the smaller  $Eu^{3+}$  ion (0.1066 nm for 8 coordination [48]) will transform to the larger  $Eu^{2+}$  ion (0.125 nm for 8 coordination [48]). On the other hand, the absorptance of blue light region decrease for samples in the range of  $0.03 \leq y \leq 0.05$  due to the decrease in crystallinity. As a result, the  $(Ca_{0.87}Eu_{0.10}Zn_{0.03})_2Al_2SiO_{7+\delta}$  pigment absorbed the blue light region, which is complementary region of yellow color, most efficiently.

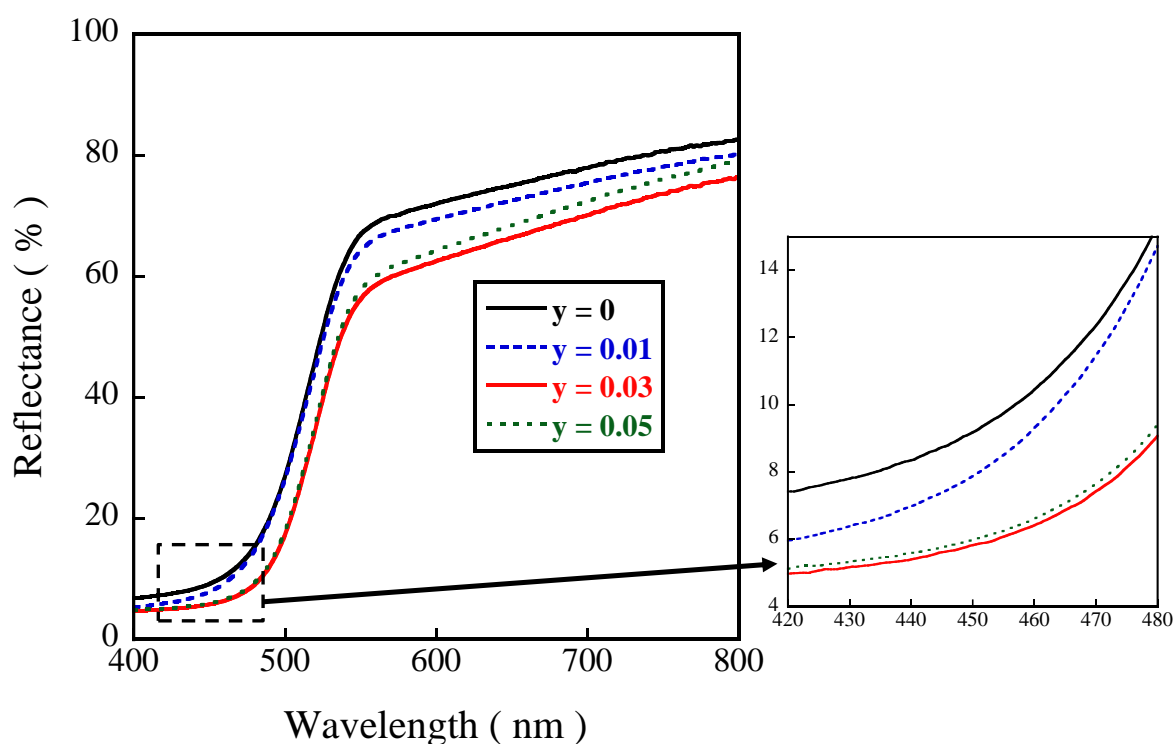


**Figure 1.1.5** UV-Vis diffuse reflectance spectra of the  $(Ca_{0.90-y}Eu_{0.10}Zn_y)_2Al_2SiO_{7+\delta}$  ( $0 \leq y \leq 0.05$ ) pigments.

In order to confirm the change of the  $\text{Eu}^{2+}$  ion concentration by doping  $\text{Zn}^{2+}$  ion into the  $\text{Ca}^{2+}$  site in the solid, XPS spectra were measured for the  $(\text{Ca}_{0.90}\text{Eu}_{0.10})_2\text{Al}_2\text{SiO}_{7+\delta}$  and  $(\text{Ca}_{0.87}\text{Eu}_{0.10}\text{Zn}_{0.03})_2\text{Al}_2\text{SiO}_{7+\delta}$  pigments (**Figure 1.1.6**), and the proportion of  $\text{Eu}^{2+}$  and  $\text{Eu}^{3+}$  ion for total Eu ion in the prepared pigments estimated from the peak area of Eu  $d_{5/2}$  peaks for divalent  $\text{Eu}^{2+}$  and trivalent  $\text{Eu}^{3+}$  [49, 50] are listed in **Table 1.1.2**. Although the  $\text{Eu}^{2+}$  ion ratio in the  $(\text{Ca}_{0.90}\text{Eu}_{0.10})_2\text{Al}_2\text{SiO}_{7+\delta}$  solid was 21%, it increased up to 24% for the  $(\text{Ca}_{0.87}\text{Eu}_{0.10}\text{Zn}_{0.03})_2\text{Al}_2\text{SiO}_{7+\delta}$  solid, and the increase concentration of  $\text{Eu}^{2+}$  ion (3%) is exactly equal to the doped concentration of  $\text{Zn}^{2+}$ . this result supports the idea that divalent  $\text{Eu}^{2+}$  concentration was increased to release the crystal strain caused by the doped  $\text{Zn}^{2+}$  ion.

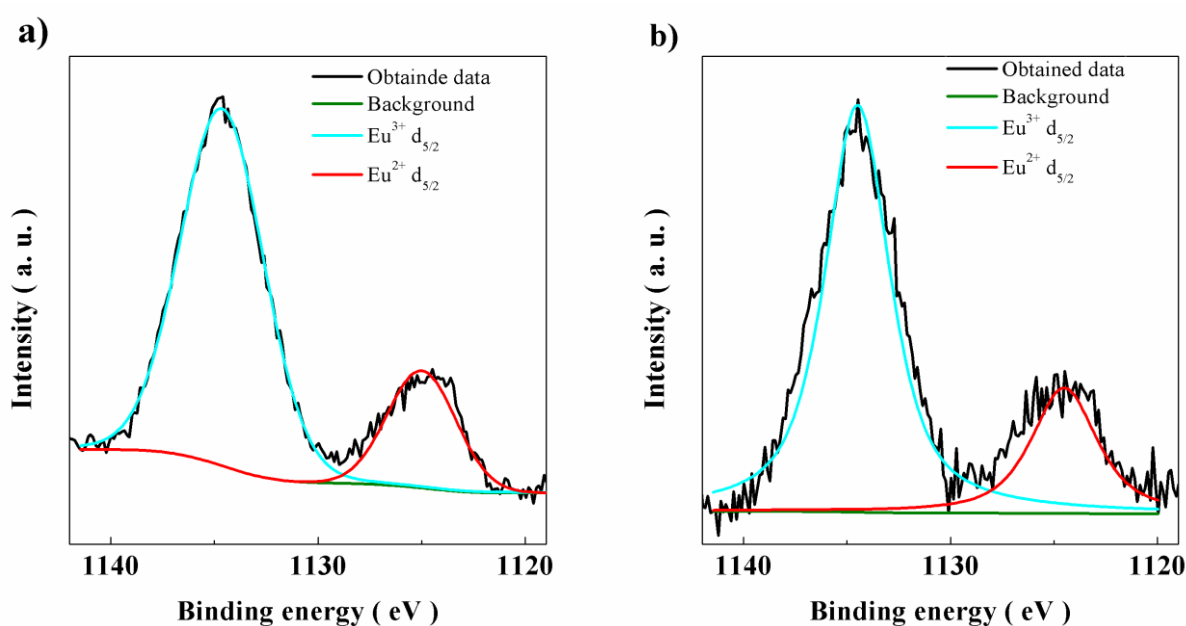


**Figure 1.1.6** XPS spectra for the  $(\text{Ca}_{0.90}\text{Eu}_{0.10})_2\text{Al}_2\text{SiO}_{7+\delta}$  (a) and  $(\text{Ca}_{0.87}\text{Eu}_{0.10}\text{Zn}_{0.03})_2\text{Al}_2\text{SiO}_{7+\delta}$  (b) pigments.

**Table 1.1.2** Concentration ratio of  $\text{Eu}^{2+}$  and  $\text{Eu}^{3+}$  in  $(\text{Ca}_{0.90}\text{Eu}_{0.10})_2\text{Al}_2\text{SiO}_{7+\delta}$  and  $(\text{Ca}_{0.87}\text{Eu}_{0.10}\text{Zn}_{0.03})_2\text{Al}_2\text{SiO}_{7+\delta}$  pigments

| Samples  | Concentration ratio ( % ) |                  |
|--|---------------------------|------------------|
|  | $\text{Eu}^{2+}$          | $\text{Eu}^{3+}$ |
| $(\text{Ca}_{0.90}\text{Eu}_{0.10})_2\text{Al}_2\text{SiO}_{7+\delta}$                 | 21                        | 79               |
| $(\text{Ca}_{0.87}\text{Eu}_{0.10}\text{Zn}_{0.03})_2\text{Al}_2\text{SiO}_{7+\delta}$ | 24                        | 76               |

The color parameters of the  $(\text{Ca}_{0.90-y}\text{Eu}_{0.10}\text{Zn}_y)_2\text{Al}_2\text{SiO}_{7+\delta}$  ( $0 \leq y \leq 0.05$ ) samples are tabulated in **Table 1.1.3**. The yellow chromaticity ( $b^*$ ) increased with increasing the amount of  $\text{Zn}^{2+}$  ion for  $0 \leq y \leq 0.03$ , as same as the result of UV-visible diffuse reflectance spectra measurements, and  $(\text{Ca}_{0.87}\text{Eu}_{0.10}\text{Zn}_{0.03})_2\text{Al}_2\text{SiO}_{7+\delta}$  pigment showed the highest  $b^*$  and  $C$  values ( $b^* = +75.8$ ,  $C = 75.8$ ) among the prepared pigments.

**Table 1.1.3** Color parameters for the  $(\text{Ca}_{0.90-y}\text{Eu}_{0.10}\text{Zn}_y)_2\text{Al}_2\text{SiO}_{7+\delta}$  ( $0 \leq y \leq 0.05$ ) pigments

| Pigments   | $L^*$ | $a^*$ | $b^*$ | $C$  | $H^\circ$ |
|--|-------|-------|-------|------|-----------|
| $(\text{Ca}_{0.90}\text{Eu}_{0.10})_2\text{Al}_2\text{SiO}_{7+\delta}$                 | 83.0  | -4.2  | +70.5 | 70.6 | 93.4°     |
| $(\text{Ca}_{0.89}\text{Eu}_{0.10}\text{Zn}_{0.01})_2\text{Al}_2\text{SiO}_{7+\delta}$ | 79.6  | -2.0  | +71.5 | 71.5 | 91.6°     |
| $(\text{Ca}_{0.87}\text{Eu}_{0.10}\text{Zn}_{0.03})_2\text{Al}_2\text{SiO}_{7+\delta}$ | 74.5  | -0.1  | +75.8 | 75.8 | 90.1°     |
| $(\text{Ca}_{0.85}\text{Eu}_{0.10}\text{Zn}_{0.05})_2\text{Al}_2\text{SiO}_{7+\delta}$ | 76.9  | -1.1  | +73.7 | 73.7 | 90.9°     |

#### 1.1.4 Conclusion

$(\text{Ca}_{1-x-y}\text{Eu}_x\text{Zn}_y)_2\text{Al}_2\text{SiO}_{7+\delta}$  ( $0 < x \leq 0.15$ ;  $0 \leq y \leq 0.05$ ) pigments were successfully synthesized as novel environmentally friendly inorganic yellow pigments. The color of the

pigments depended on the concentrations of  $\text{Eu}^{2+}$  and  $\text{Zn}^{2+}$  ions. Since the  $(\text{Ca}_{0.87}\text{Eu}_{0.10}\text{Zn}_{0.03})_2\text{Al}_2\text{SiO}_{7+\delta}$  pigment showed the most vivid yellow hue, color parameters of which were  $L^* = 74.5$ ,  $a^* = -0.1$ ,  $b^* = +75.8$ ,  $C = 75.8$ , and  $H^\circ = 90.1$ , the present pigment that composed of only nontoxic elements is expected to be an effective alternative for the conventional toxic pigments.

## Chapter 1.2

# Novel Environmentally Friendly Yellow Pigments Based on Rare Earth Tungstate ( $\text{Ln}_2\text{W}_2\text{O}_9$ ; Ln = Pr, Sm, Gd)

### 1.2.1 Introduction

The synthesis of yellow pigments base on Gehlenite-type structure was described in **Chapter 1.1**. Another kind of yellow pigment was attempted to be synthesise using rare earth ion as a colorant. Rare earth tungstates  $\text{Ln}_2\text{W}_2\text{O}_9$  (Ln =  $\text{Pr}^{3+}$ ,  $\text{Sm}^{3+}$ , and  $\text{Gd}^{3+}$ ) and  $\text{Ce}^{3+}$  ion were selected as base materials and colorant, respectively. The rare earth elements ( $\text{Pr}^{3+}$ ,  $\text{Sm}^{3+}$ ,  $\text{Gd}^{3+}$ , and  $\text{Ce}^{3+}$ ) are non-toxic elements, and  $\text{Pr}_2\text{W}_2\text{O}_9$ ,  $\text{Sm}_2\text{W}_2\text{O}_9$ , and  $\text{Gd}_2\text{W}_2\text{O}_9$  have the same crystal structure (monoclinic) and space group ( $P2_1/c$ ). Furthermore, rare earth elements have similar ionic radius to each other, so  $\text{Ce}^{3+}$  ion can replace the  $\text{Ln}^{3+}$  ions in the  $\text{Ln}_2\text{W}_2\text{O}_9$ . By the way, tungstate materials widely used for pigment materials due to their optical property [51-53], are known to show the broad optical absorption band until near-UV visible region caused by the charge transfer (CT) transitions of  $(\text{WO}_4)^{2-}$  and  $(\text{WO}_6)^{6-}$  oxyanion complex, resulting in showing green to yellow color. In addition,  $\text{Ce}^{3+}$  ion, which has  $4f^1$ - $5d^1$  transition band, acts as a colorant because it can absorb in the visible light region under around 500 nm by interpolating into the band gap of host material [54].

In order to develop the inorganic yellow pigment, the  $\text{Ln}^{3+}$  ( $\text{Pr}^{3+}$ ,  $\text{Sm}^{3+}$ , and  $\text{Gd}^{3+}$ ) ion in the  $\text{Ln}_2\text{W}_2\text{O}_9$  lattice was partially substituted with  $\text{Ce}^{3+}$  and  $\text{Tb}^{3+}$  ion. In **Chapter 1.1**, it was identified that increase in concentration for colorant positively affects the color properties, Furthermore,  $\text{Tb}^{3+}$  ion with smaller ionic radius than that of  $\text{Ln}^{3+}$  ion makes larger split of  $4f^1$ - $5d^1$  energy level for  $\text{Ce}^{3+}$  ion. Therefore, the concentration of  $\text{Ce}^{3+}$  ion was optimized to identify the relationship between concentration of colorant and absorptance. Furthermore, the

concentration of  $Tb^{3+}$  ion was also optimized to clarify the relationship between crystal field around colorant ion and band gap change.

## 1.2.2 Experimental Procedure

The  $(Ln_{1-x}Ce_x)_2W_2O_{9+\delta}$  ( $Ln = Pr^{3+}$ ,  $Sm^{3+}$ , and  $Gd^{3+}$ ), and  $(Gd_{1-x}Ce_xTb_y)_2W_2O_{9+\delta}$  ( $0 \leq x \leq 0.30$ ;  $0 \leq y \leq 0.03$ ) samples were synthesized by the conventional solid state reaction method. The stoichiometric amounts of  $Pr_6O_{11}$ ,  $Sm_2O_3$ ,  $Gd_2O_3$ ,  $CeO_2$ ,  $Tb_4O_7$ , and  $WO_3$  powder were mixed by agate mortar, being followed by mixing with planetary ball milling apparatus (Pulverisette 7 premium line, FRITSCHE GmbH) at 300 rpm for 3h. The homogeneous mixture was calcined twice at 1000 °C for 15 h under atmospheric air, and it was then finally calcined at 1100 °C for 15 h under atmospheric air. The calcined mixture was ground at the end of each calcination processing in the agate mortar.

The result of X-ray fluorescence spectroscopy (XRF; Rigaku, ZSX-100e), which reveals the samples composition, indicated the good agreement with the nominal stoichiometric composition. The samples were examined by X-ray powder diffraction (XRD; SmartLab, Rigaku) using  $Cu-K\alpha$  radiation (40 kV and 30 mA) to identify their crystal structures. Rietveld refinement analysis was performed to clarify the crystallographic data of the samples by using the RIETAN-FP program [55], and the crystal structures of samples were illustrated by the VESTA program [56]. The lattice volume was estimated from the XRD peak angles. X-ray photoelectron spectroscopy (XPS; PHI5000 VersaProbe II, ULVAC-PHI) was carried out at room temperature using an  $Al-K\alpha$  radiation (1486.6 eV). The effect of charging on the binding energies was corrected with respect to the C 1S peak at 284.6 eV.

The optical reflectance spectrum measurement was measured using a UV-vis spectroscopy (UV-2600, Shimadzu) with barium sulfate as a reference. The band gap energies of the samples were determined from the absorption edge of the absorbance spectra by the

Kubelka-Munk theory,  $f(R) = (1 - R)^2/2R$ , where R is reflectance [57, 58]. The color properties of the samples were estimated in terms of the CIE  $L^*a^*b^*$  system with a colorimeter (CR-400, Konica-Minolta). In this system, the parameter  $L^*$  represents the brightness (100) or darkness (0) in a neutral gray scale, and the parameters  $a^*$  [red (+) - green axis (-)] and  $b^*$  [yellow (+) - blue axis (-)] indicate the color, respectively. The chroma parameter (C) presenting the color saturation of the pigment was obtained by the formula ( $C = [(a^*)^2 + (b^*)^2]^{1/2}$ ). The parameter  $H^\circ$  (hue angle) which ranges from 0 to 360° was calculated according to the following equation,  $H^\circ = \tan^{-1}(b^*/a^*)$ ; ( $H^\circ = 90^\circ$  was for pure yellow color).

### 1.2.3 Results and Discussion

#### 1.2.3.1 $(\text{Ln}_{1-x}\text{Ce}_x)_2\text{W}_2\text{O}_{9+\delta}$ (Ln = $\text{Pr}^{3+}$ , $\text{Sm}^{3+}$ , $\text{Gd}^{3+}$ )

**Figure 1.2.1** shows the representative XRD patterns of the  $(\text{Ln}_{1-x}\text{Ce}_x)_2\text{W}_2\text{O}_{9+\delta}$  (Ln =  $\text{Pr}^{3+}$ ,  $\text{Sm}^{3+}$ , and  $\text{Gd}^{3+}$ ) samples. The diffraction patterns were all in good agreement with a single phase of the monoclinic phase without formation of any impurity. UV-vis diffuse reflectance spectra for the  $(\text{Ln}_{1-x}\text{Ce}_x)_2\text{W}_2\text{O}_{9+\delta}$  samples are depicted in **Figure 1.2.2**. The  $(\text{Ln}_{1-x}\text{Ce}_x)_2\text{W}_2\text{O}_{9+\delta}$  (Ln =  $\text{Pr}^{3+}$ ,  $\text{Sm}^{3+}$ , and  $\text{Gd}^{3+}$ ) samples showed strong optical absorption under around 500 nm, which includes blue light region (435 ~ 480 nm) as a complementary color of yellow, due to the  $4f^1-5d^1$  transition of  $\text{Ce}^{3+}$  ion [54]. The absorption edge of  $(\text{Ln}_{1-x}\text{Ce}_x)_2\text{W}_2\text{O}_{9+\delta}$  (Ln =  $\text{Sm}^{3+}$ , or  $\text{Gd}^{3+}$ ) samples shifted to longer wavelength direction with increasing Ce ion contents from 0.10 to 0.15. This phenomenon is exactly similar with previous result given in **chapter 1.1** that the concentration of colorant and absorbance are directly proportional.

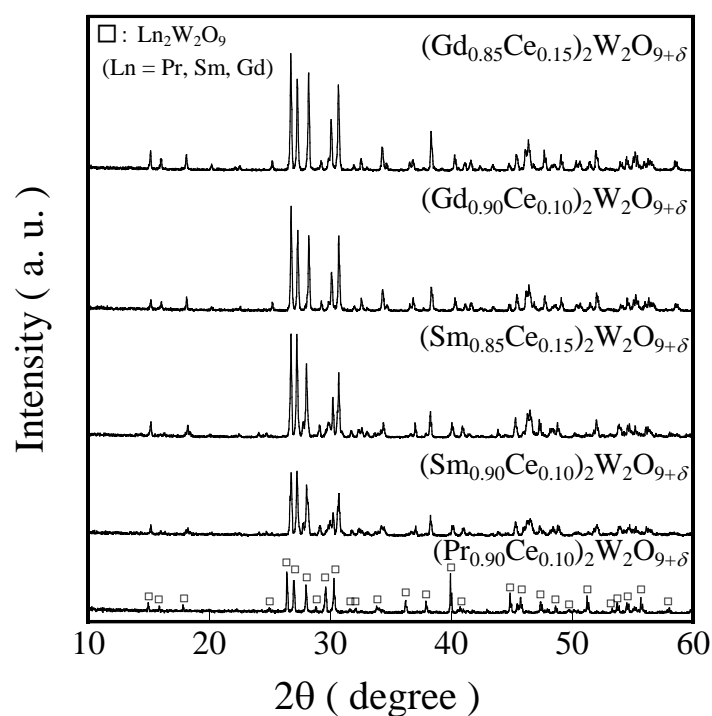


**Figure 1.2.1** XRD patterns of the  $(\text{Ln}_{1-x}\text{Ce}_x)_2\text{W}_2\text{O}_{9+\delta}$  ( $\text{Ln} = \text{Pr}^{3+}$ ,  $\text{Sm}^{3+}$ , and  $\text{Gd}^{3+}$ ) samples.

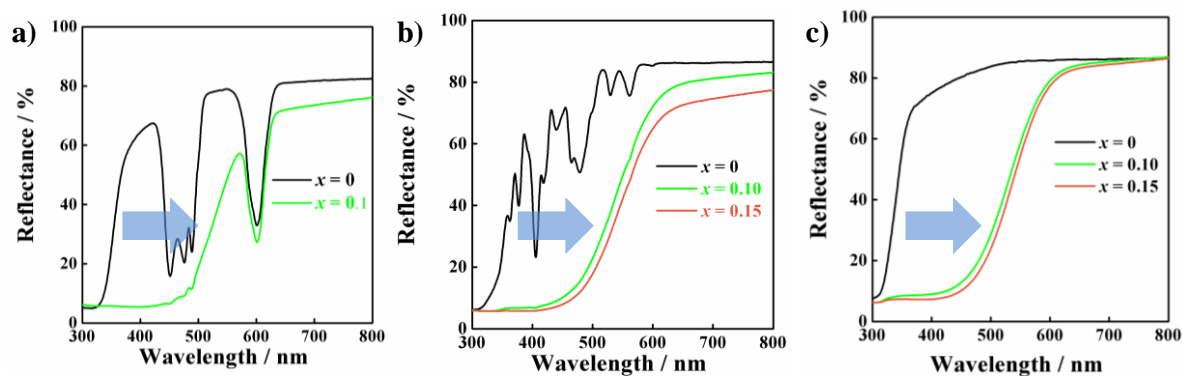


**Figure 1.2.2** UV-Vis diffuse reflectance spectra for a)  $(\text{Pr}_{1-x}\text{Ce}_x)_2\text{W}_2\text{O}_{9+\delta}$ , b)  $(\text{Sm}_{1-x}\text{Ce}_x)_2\text{W}_2\text{O}_{9+\delta}$ , and c)  $(\text{Gd}_{1-x}\text{Ce}_x)_2\text{W}_2\text{O}_{9+\delta}$  samples.

The color parameters of the  $(\text{Ln}_{1-x}\text{Ce}_x)_2\text{W}_2\text{O}_{9+\delta}$  ( $\text{Ln} = \text{Pr}^{3+}$ ,  $\text{Sm}^{3+}$ , and  $\text{Gd}^{3+}$ ) samples are tabulated in **Table 1.2.1**.  $\text{Pr}_2\text{W}_2\text{O}_9$  sample showed the light green color, and  $\text{Ln}_2\text{W}_2\text{O}_{9+\delta}$  ( $\text{Ln} = \text{Sm}^{3+}$ , and  $\text{Gd}^{3+}$ ) samples showed white color. After Ce ion doping, the color turned from light green or white to yellow, which are originated from  $4f^1-5d^1$  transition of  $\text{Ce}^{3+}$  ion [54], and  $(\text{Ln}_{0.85}\text{Ce}_{0.15})_2\text{W}_2\text{O}_{9+\delta}$  ( $\text{Ln} = \text{Sm}^{3+}$ , and  $\text{Gd}^{3+}$ ) pigments exhibited the higher  $b^*$  values than those of  $(\text{Ln}_{0.90}\text{Ce}_{0.10})_2\text{W}_2\text{O}_{9+\delta}$  ( $\text{Ln} = \text{Sm}^{3+}$ , and  $\text{Gd}^{3+}$ ) pigments. As a result, the  $(\text{Gd}_{0.85}\text{Ce}_{0.15})_2\text{W}_2\text{O}_{9+\delta}$  pigment showed the highest yellow hue among the prepared samples.

**Table 1.2.1** Color parameters for the  $(\text{Ln}_{1-x}\text{Ce}_x)_2\text{W}_2\text{O}_{9+\delta}$  ( $\text{Ln} = \text{Pr}^{3+}$ ,  $\text{Sm}^{3+}$ , and  $\text{Gd}^{3+}$ ) samples

| Pigments  | $L^*$ | $a^*$ | $b^*$ | $C$  | $H^\circ$ |
|---|-------|-------|-------|------|-----------|
| $\text{Pr}_2\text{W}_2\text{O}_9$                                   | 89.6  | -23.6 | +36.3 | 43.3 | 123.0°    |
| $(\text{Pr}_{0.90}\text{Ce}_{0.10})_2\text{W}_2\text{O}_{9+\delta}$ | 67.0  | +2.7  | +61.6 | 61.7 | 87.5°     |
| $\text{Sm}_2\text{W}_2\text{O}_9$                                   | 96.0  | -2.2  | +17.6 | 17.7 | 97.1      |
| $(\text{Sm}_{0.90}\text{Ce}_{0.10})_2\text{W}_2\text{O}_{9+\delta}$ | 80.0  | +10.6 | +60.8 | 61.7 | 80.1°     |
| $(\text{Sm}_{0.85}\text{Ce}_{0.15})_2\text{W}_2\text{O}_{9+\delta}$ | 76.0  | +13.4 | +61.9 | 63.3 | 77.8°     |
| $\text{Gd}_2\text{W}_2\text{O}_9$                                   | 98.5  | -0.9  | +4.0  | 4.1  | 102.7°    |
| $(\text{Gd}_{0.90}\text{Ce}_{0.10})_2\text{W}_2\text{O}_{9+\delta}$ | 83.0  | +7.3  | +58.7 | 59.2 | 82.9°     |
| $(\text{Gd}_{0.85}\text{Ce}_{0.15})_2\text{W}_2\text{O}_{9+\delta}$ | 80.7  | +9.4  | +62.3 | 63.0 | 81.4°     |

### 1.2.3.2 $(\text{Gd}_{1-x}\text{Ce}_x)_2\text{W}_2\text{O}_{9+\delta}$ ( $0 \leq x \leq 0.30$ )

Since the  $(\text{Gd}_{1-x}\text{Ce}_x)_2\text{W}_2\text{O}_{9+\delta}$  ( $x = 0.10$  and  $0.15$ ) solids were confirmed to show the high yellow hue among the prepared samples, the concentration of replaced  $\text{Ce}^{3+}$  ion was optimized to increase their yellowness. **Figure 1.2.3** shows representative XRD patterns for  $(\text{Gd}_{1-x}\text{Ce}_x)_2\text{W}_2\text{O}_{9+\delta}$  ( $0 \leq x \leq 0.30$ ) samples. All the XRD patterns were attributed to be single-phase of monoclinic structure in the  $x$  range of 0 to 0.20, and no impurities phase was observed.

However,  $(\text{Gd}_{0.70}\text{Ce}_{0.30})_2\text{W}_2\text{O}_{9+\delta}$  solid was obtained as the two-phase mixture of  $\text{Gd}_2\text{W}_2\text{O}_9$  and  $\text{Gd}_2\text{W}_3\text{O}_{12}$ . The lattice volume for the  $(\text{Gd}_{1-x}\text{Ce}_x)_2\text{W}_2\text{O}_{9+\delta}$  ( $0 \leq x \leq 0.30$ ) samples, which were calculated from the diffraction peak angles in the XRD patterns, is depicted in **Figure 1.2.4**. The lattice volume increased linearly with increasing the Ce content in the range of single-phase region ( $0 \leq x \leq 0.20$ ), which indicates that Ce ion was successfully replaced the  $\text{Gd}^{3+}$  ion in the  $\text{Gd}_2\text{W}_2\text{O}_9$  lattice. Whereas, the lattice volume was nearly constant in the range of two-phase mixture region ( $x > 0.20$ ). This result strongly indicates that the solubility limit of Ce ion in  $\text{Gd}_2\text{W}_2\text{O}_9$  lattice is  $x = 0.2$ .

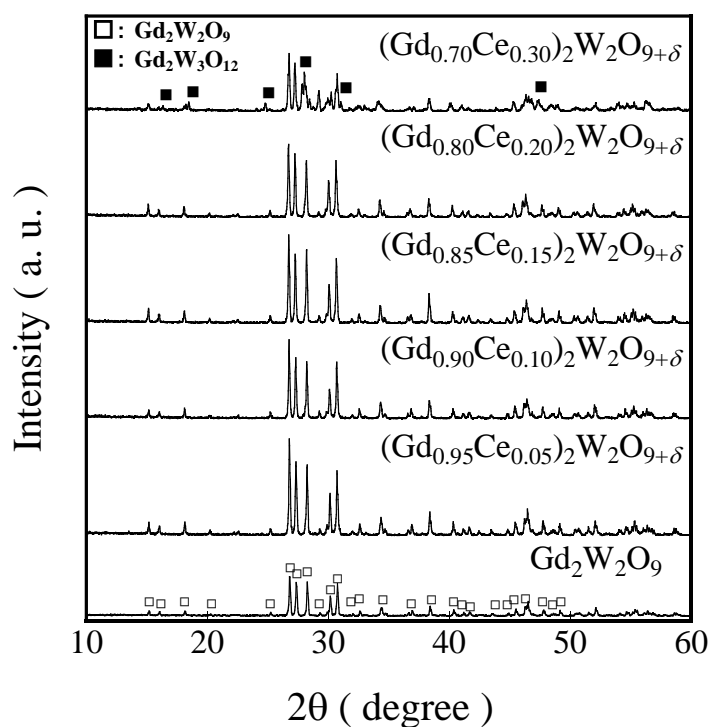


**Figure 1.2.3** XRD patterns of the  $(\text{Gd}_{0.70}\text{Ce}_{0.30})_2\text{W}_2\text{O}_{9+\delta}$  ( $0 \leq x \leq 0.30$ ) samples.

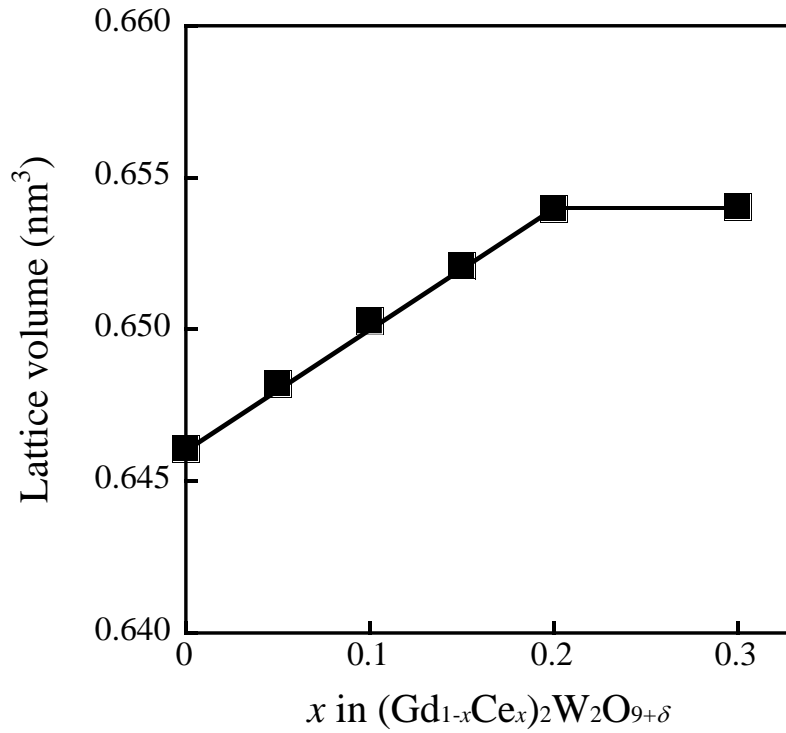


**Figure 1.2.4** Change in lattice volume for  $(\text{Gd}_{1-x}\text{Ce}_x)_2\text{W}_2\text{O}_{9+\delta}$  ( $0 \leq x \leq 0.30$ ) samples as a function of  $x$ .

In order to identify the valance state of Ce ion in the  $(\text{Gd}_{0.80}\text{Ce}_{0.20})_2\text{W}_2\text{O}_{9+\delta}$  having the solid solubility composition, XPS analysis conducted. **Figure 1.2.5** shows the measured Ce 3d XPS spectra. The Ce 3d XPS spectra of  $(\text{Gd}_{0.80}\text{Ce}_{0.20})_2\text{W}_2\text{O}_{9+\delta}$  indicate that it is composed with two spin-orbit multiplets ( $v$  and  $u$ ) originated from the  $3d_{3/2}$  and  $3d_{5/2}$  core-levels with a splitting energy of  $\sim 18.3$  eV [59, 60]. The main peaks at  $v'$  and  $u'$  (886.2 and 904.5 eV), and satellite peaks at  $v_0$  and  $u_0$  (881.2 and 900.5 eV) are corresponding to the  $3d^9 4f^1$  and  $3d^9 4f^2$  states of the  $\text{Ce}^{3+}$  ion. The peaks at  $v$ ,  $v''$ ,  $u$ ,  $u''$ , and  $u'''$  (884.1, 899.1, 902.8, 906.4, and 916.8 eV) are corresponded to  $\text{Ce}^{4+}$ . In addition, the peaks at  $v'''$  and  $u'''$  (899.1 and 916.8 eV) are corresponded to the  $3d^9 4f^0$  final state, and the peaks at  $v$ ,  $u$ , and  $u''$  (884.1, 902.8, and 906.4 eV) are corresponded to the  $3d^9 4f^2$  and  $3d^9 4f^1$  final states [61]. The concentration ratio of  $\text{Ce}^{3+}$  and  $\text{Ce}^{4+}$

ion in  $(\text{Gd}_{0.80}\text{Ce}_{0.20})_2\text{W}_2\text{O}_{9+\delta}$  pigment estimated from the areas of the fitted XPS curve are listed in **Table 1.2.2**. It showed that the concentration ratio of  $\text{Ce}^{3+}$  and  $\text{Ce}^{4+}$  ion is almost same, which are 51% and 49%, respectively.

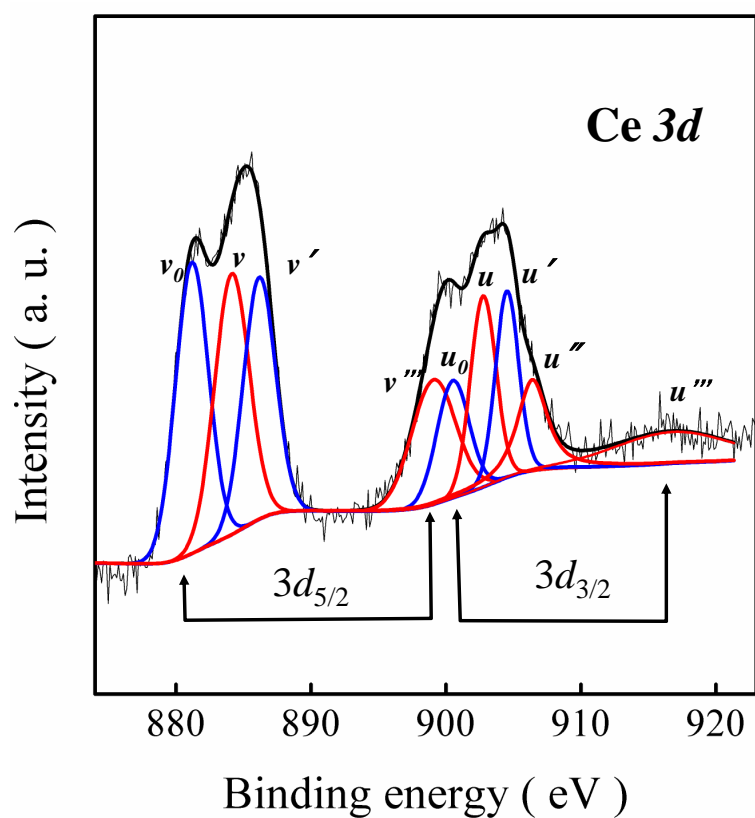


**Figure 1.2.5** XPS spectrum for  $(\text{Gd}_{0.80}\text{Ce}_{0.20})_2\text{W}_2\text{O}_{9+\delta}$  pigment.

**Table 1.2.2** Concentration ratio of  $\text{Ce}^{3+}$  and  $\text{Ce}^{4+}$  ion for the  $(\text{Gd}_{0.80}\text{Ce}_{0.20})_2\text{W}_2\text{O}_{9+\delta}$  pigment

| sample  | Concentration ratio / % |                  |
|---|-------------------------|------------------|
|   | $\text{Ce}^{3+}$        | $\text{Ce}^{4+}$ |
| $(\text{Gd}_{0.80}\text{Ce}_{0.20})_2\text{W}_2\text{O}_{9+\delta}$ | 51                      | 49               |

**Figure 1.2.6** illustrates the UV-vis diffuse reflectance spectra for  $(\text{Gd}_{1-x}\text{Ce}_x)_2\text{W}_2\text{O}_{9+\delta}$  ( $0 \leq x \leq 0.30$ ) samples. The absorption edge was significantly shifted to longer wavelength direction due to the  $4f^1-5d^1$  transition of  $\text{Ce}^{3+}$  [54], which is proved from the XPS result. All samples without  $\text{Gd}_2\text{W}_2\text{O}_9$  exhibited strong optical absorption in the blue light region (435 ~ 480 nm) as a complementary color region. As a result,  $(\text{Gd}_{0.80}\text{Ce}_{0.20})_2\text{W}_2\text{O}_{9+\delta}$  pigment absorbed most efficiently in the blue light region (435 ~ 480 nm), and this result attests that the absorptance is proportional to concentration of colorant in the range of single-phase region.

The color parameters of the  $(\text{Gd}_{1-x}\text{Ce}_x)_2\text{W}_2\text{O}_{9+\delta}$  ( $0 \leq x \leq 0.30$ ) samples are summarized in **Table 1.2.1**. The  $(\text{Gd}_{0.80}\text{Ce}_{0.20})_2\text{W}_2\text{O}_{9+\delta}$  pigment showed the vivid yellow hue ( $b^* = +63.5$ ) among the prepared samples.

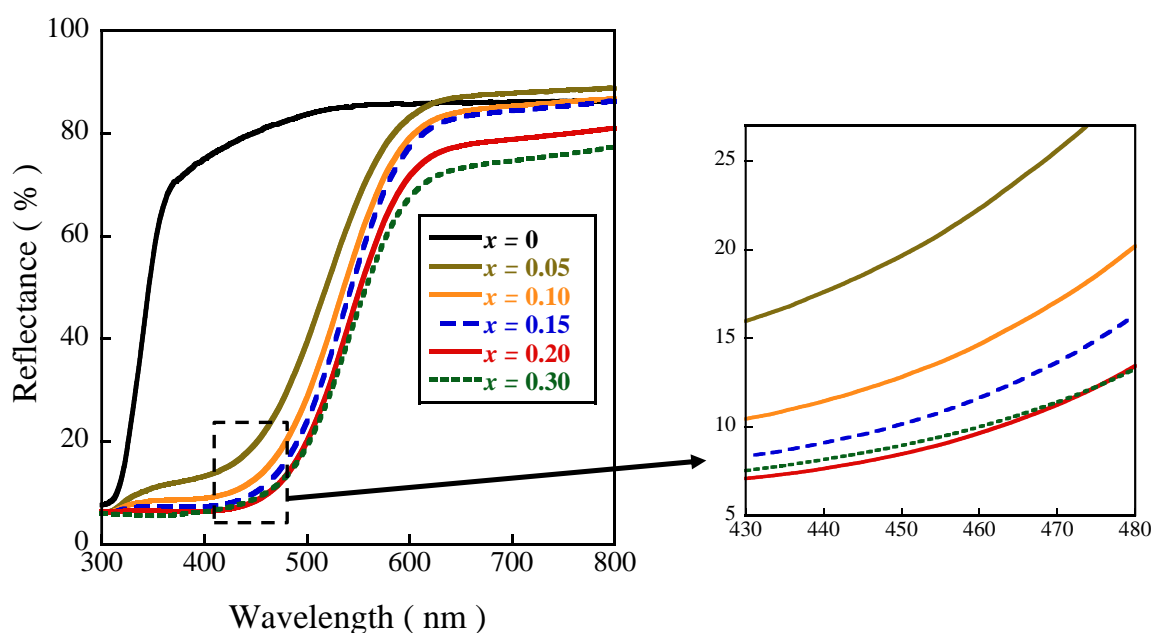


**Figure 1.2.6** UV-Vis diffuse reflectance spectra for  $(\text{Gd}_{1-x}\text{Ce}_x)_2\text{W}_2\text{O}_{9+\delta}$  ( $0 \leq x \leq 0.30$ ) samples.

**Table 1.2.2** Color parameters for  $(\text{Gd}_{1-x}\text{Ce}_x)_2\text{W}_2\text{O}_{9+\delta}$  ( $0 \leq x \leq 0.30$ ) samples

| Samples   | $L^*$ | $a^*$ | $b^*$ | $C$  | $H^\circ$ |
|---|-------|-------|-------|------|-----------|
| $\text{Gd}_2\text{W}_2\text{O}_9$                                   | 98.5  | -0.9  | +4.0  | 4.1  | 102.7°    |
| $(\text{Gd}_{0.95}\text{Ce}_{0.05})_2\text{W}_2\text{O}_{9+\delta}$ | 87.1  | +3.1  | +50.7 | 50.8 | 86.5°     |
| $(\text{Gd}_{0.90}\text{Ce}_{0.10})_2\text{W}_2\text{O}_{9+\delta}$ | 83.0  | +7.3  | +58.7 | 59.2 | 82.9°     |
| $(\text{Gd}_{0.85}\text{Ce}_{0.15})_2\text{W}_2\text{O}_{9+\delta}$ | 80.7  | +9.4  | +62.3 | 63.0 | 81.4°     |
| $(\text{Gd}_{0.80}\text{Ce}_{0.20})_2\text{W}_2\text{O}_{9+\delta}$ | 78.5  | +11.5 | +63.5 | 65.7 | 79.9°     |
| $(\text{Gd}_{0.70}\text{Ce}_{0.30})_2\text{W}_2\text{O}_{9+\delta}$ | 77.1  | +11.8 | +59.4 | 60.6 | 78.8°     |

### 1.2.3.3 $(\text{Gd}_{0.80}\text{Ce}_{0.20}\text{Tb}_y)_2\text{W}_2\text{O}_{9+\delta}$ ( $0 \leq y \leq 0.03$ )

In the previous section, the relationship between the absorbance and concentration of colorant was described. In this section, in order to further increase the yellow hue,  $\text{Gd}^{3+}$  ion was replaced by  $\text{Tb}^{3+}$  ion in  $\text{Gd}_2\text{W}_2\text{O}_9$  lattice, and the crystal field and the split of  $4f^1-5d^1$  energy level of  $\text{Ce}^{3+}$  ion were intentionally controlled. X-ray powder diffraction (XRD) patterns for the  $(\text{Gd}_{0.80}\text{Ce}_{0.20}\text{Tb}_y)_2\text{W}_2\text{O}_{9+\delta}$  ( $0 \leq y \leq 0.03$ ) pigments are shown in **Figure 1.2.7**. The XRD pattern was in good agreement with single phase of monoclinic structure for the sample in which the concentration of  $\text{Tb}^{3+}$  ion was 1 mol%. However, for the samples in which the concentration of  $\text{Tb}^{3+}$  ion was more than 2 mol%, the cubic  $\text{CeO}_2$  structure peaks were observed as impurity phase. **Figure 1.2.8** depicts the effect of  $\text{Tb}^{3+}$  ion concentration on the lattice volume of the  $(\text{Gd}_{0.80}\text{Ce}_{0.20}\text{Tb}_y)_2\text{W}_2\text{O}_{9+\delta}$  ( $0 \leq y \leq 0.03$ ) pigments. The lattice volume increased monotonically with the decrease in the  $\text{Tb}^{3+}$  ion concentration in the range of single-phase region ( $y \leq 0.01$ ), which indicates that  $\text{Tb}^{3+}$  ion partially replaced the  $\text{Gd}^{3+}$  ion in the  $\text{Gd}_2\text{W}_2\text{O}_9$  lattice because the ionic radius of  $\text{Tb}^{3+}$  ion (0.104 nm for 8 coordination [48]; 0.1095 nm for 9 coordination [48]) is smaller than that of  $\text{Gd}^{3+}$  ion (0.1053 nm for 8 coordination [48]; 0.1107 nm for 9 coordination [48]). On the other hand, the lattice volume of monoclinic structure became constant in the range of two-phase mixture region ( $y > 0.01$ ), indicating that the solid solution limit of  $\text{Tb}^{3+}$  ion is  $y = 0.01$ .

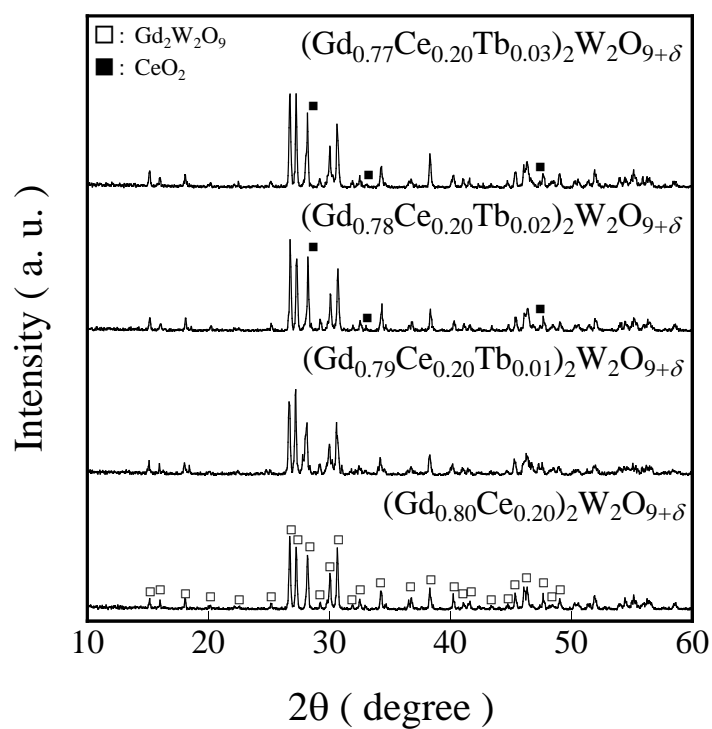


**Figure 1.2.7** XRD patterns of the  $(\text{Gd}_{0.80}\text{Ce}_{0.20}\text{Tb}_y)_2\text{W}_2\text{O}_{9+\delta}$  ( $0 \leq y \leq 0.03$ ) pigments.

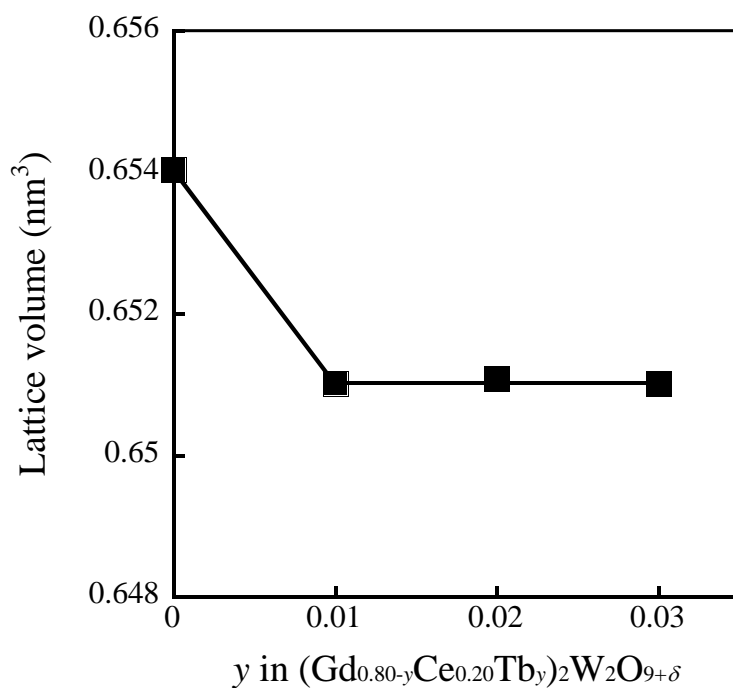


**Figure 1.2.8** Change in lattice volumes for  $(\text{Gd}_{0.80}\text{Ce}_{0.20}\text{Tb}_y)_2\text{W}_2\text{O}_{9+\delta}$  ( $0 \leq y \leq 0.03$ ) pigments as a function of  $x$ .

**Figure 1.2.9** depicts the X-ray powder diffraction data and coordination environment of Ce cations obtained by Rietveld refinement for the  $(\text{Gd}_{0.80}\text{Ce}_{0.20})_2\text{W}_2\text{O}_{9+\delta}$  and  $(\text{Gd}_{0.79}\text{Ce}_{0.20}\text{Tb}_{0.01})_2\text{W}_2\text{O}_{9+\delta}$  pigments, and average bond distance of Ce-O in  $\text{GdO}_8$  and  $\text{GdO}_9$  units for  $(\text{Gd}_{0.80}\text{Ce}_{0.20})_2\text{W}_2\text{O}_{9+\delta}$  and  $(\text{Gd}_{0.79}\text{Ce}_{0.20}\text{Tb}_{0.01})_2\text{W}_2\text{O}_{9+\delta}$  pigments are tabulated in **Table 1.2.3**. The Rietveld refinement results of  $(\text{Gd}_{0.80}\text{Ce}_{0.20})_2\text{W}_2\text{O}_{9+\delta}$  and  $(\text{Gd}_{0.79}\text{Ce}_{0.20}\text{Tb}_{0.01})_2\text{W}_2\text{O}_{9+\delta}$  pigments showed the high reliability ( $R_{\text{wp}}$ ) values, which were 12.9, and 11.8, respectively. The average bond distance of Ce-O in  $\text{GdO}_8$  and  $\text{GdO}_9$  units for  $(\text{Gd}_{0.80}\text{Ce}_{0.20})_2\text{W}_2\text{O}_{9+\delta}$  and  $(\text{Gd}_{0.79}\text{Ce}_{0.20}\text{Tb}_{0.01})_2\text{W}_2\text{O}_{9+\delta}$  pigments decreased from 0.24525 nm to 0.24517 nm, and from 0.24828 nm to 0.24823 nm, respectively.

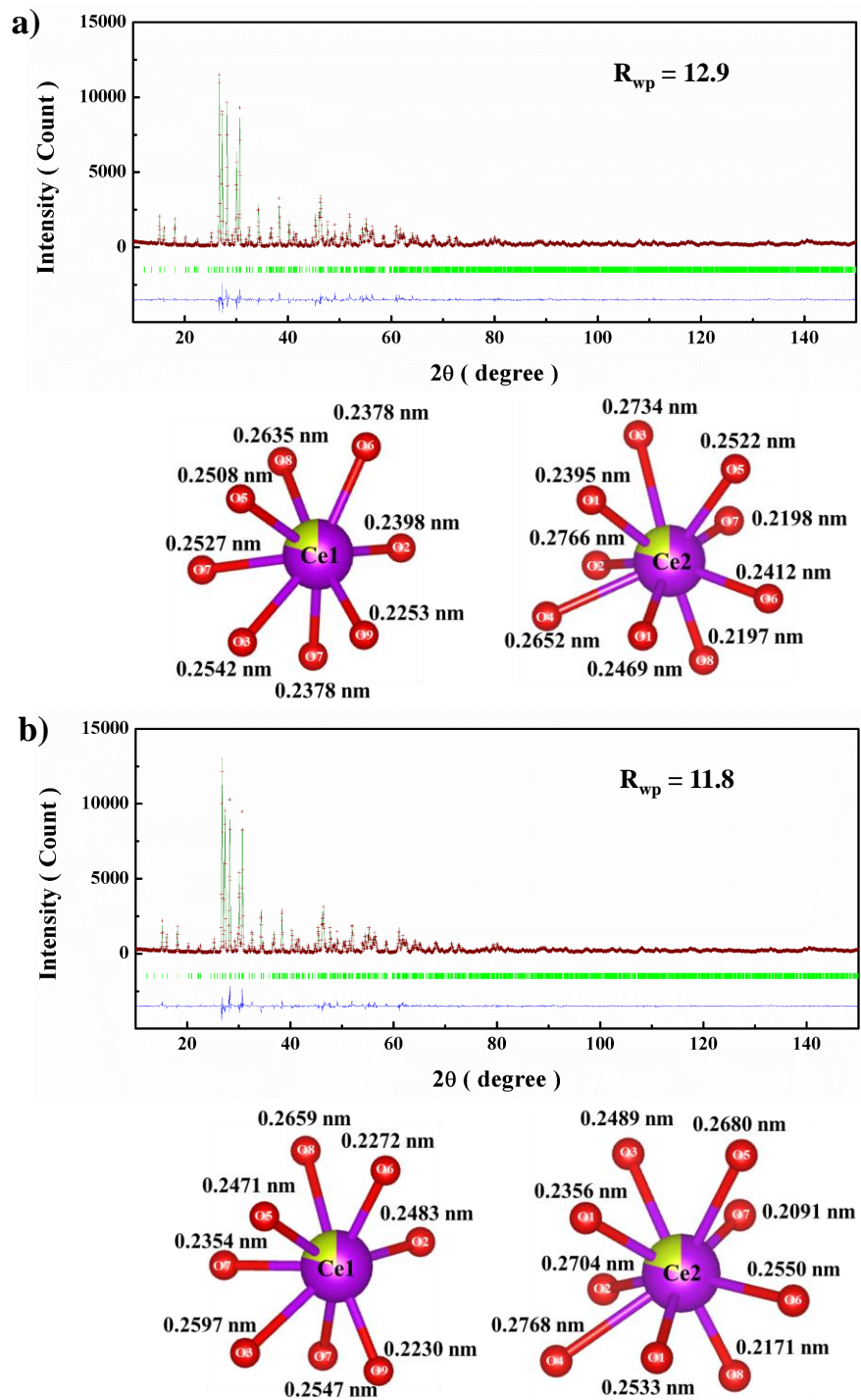


**Figure 1.2.9** Rietveld refinement result for the X-ray powder diffraction data and coordination environment of Ce cations for (a)  $(\text{Gd}_{0.80}\text{Ce}_{0.20})_2\text{W}_2\text{O}_{9+\delta}$  and (b)  $(\text{Gd}_{0.79}\text{Ce}_{0.20}\text{Tb}_{0.01})_2\text{W}_2\text{O}_{9+\delta}$  samples. Red symbol: measured pattern, green solid line: calculated pattern, blue solid line: difference between their intensities.

**Table 1.2.3** Average bond distance of Ce–O for  $(\text{Gd}_{0.80}\text{Ce}_{0.20})_2\text{W}_2\text{O}_{9+\delta}$  and  $(\text{Gd}_{0.79}\text{Ce}_{0.20}\text{Tb}_{0.01})_2\text{W}_2\text{O}_{9+\delta}$  pigments

|   | Ce–O average bond distance / nm |                  |
|---|---------------------------------|------------------|
|   | GdO <sub>8</sub>                | GdO <sub>9</sub> |
| $(\text{Gd}_{0.80}\text{Ce}_{0.20})_2\text{W}_2\text{O}_{9+\delta}$                 | 0.24525                         | 0.24828          |
| $(\text{Gd}_{0.79}\text{Ce}_{0.20}\text{Tb}_{0.01})_2\text{W}_2\text{O}_{9+\delta}$ | 0.24463                         | 0.24789          |

The UV-vis diffuse reflectance spectra for the  $(\text{Gd}_{0.80-y}\text{Ce}_{0.20}\text{Tb}_y)_2\text{W}_2\text{O}_{9+\delta}$  ( $0 \leq y \leq 0.03$ ) pigments are illustrated in **Figure 1.2.10**.  $(\text{Gd}_{0.79}\text{Ce}_{0.20}\text{Tb}_{0.01})_2\text{W}_2\text{O}_{9+\delta}$  pigment showed the highest absorptance in the blue light region (435 nm ~ 485 nm) as a complementary color region among the prepared pigments.

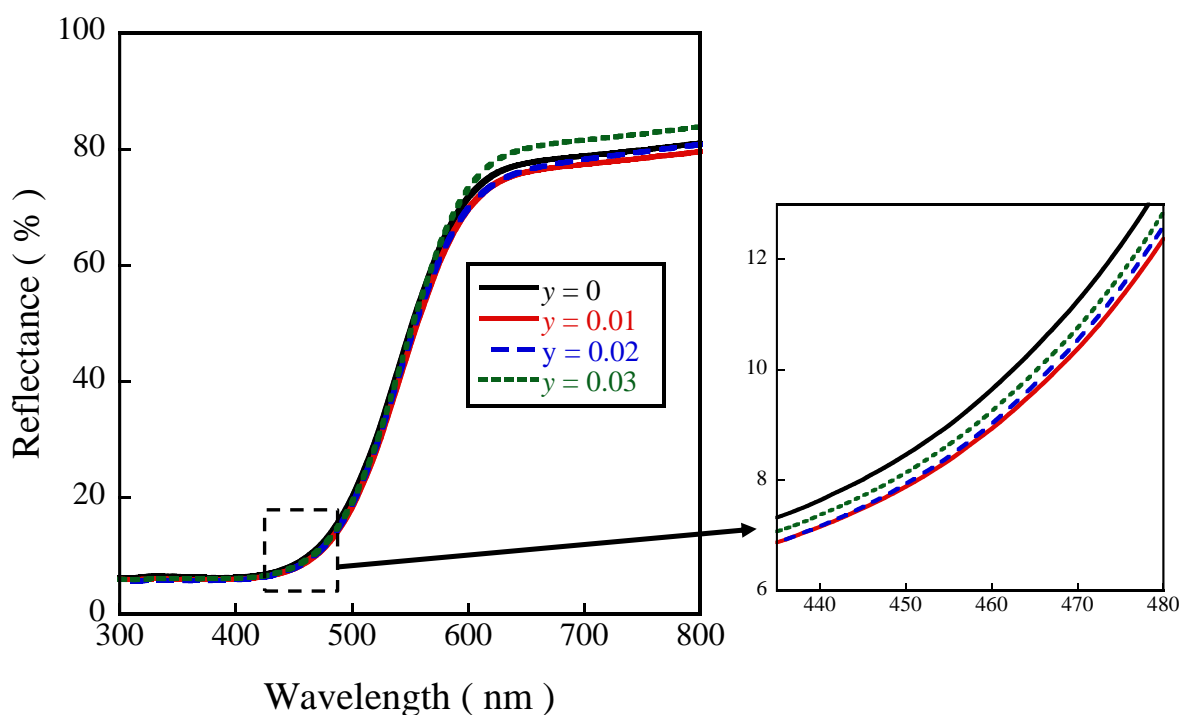


**Figure 1.2.10** UV-Vis diffuse reflectance spectra for  $(\text{Gd}_{0.80-y}\text{Ce}_{0.20}\text{Tb}_y)_2\text{W}_2\text{O}_{9+\delta}$  ( $0 \leq y \leq 0.03$ ) pigments.

**Figure 1.2.11** shows the extracted optical band gaps for the  $(\text{Gd}_{0.80-y}\text{Ce}_{0.20}\text{Tb}_y)_2\text{W}_2\text{O}_{9+\delta}$  ( $y = 0$  and  $0.01$ ) pigments, and the color parameters and band gap energies of the  $(\text{Gd}_{0.80-y}\text{Ce}_{0.20}\text{Tb}_y)_2\text{W}_2\text{O}_{9+\delta}$  ( $0 \leq y \leq 0.03$ ) pigments are listed in **Table 1.2.4**. The optical band gap was extracted from the absorbance data by using the Kubelka-Munk theory, and it was confirmed that the band gap energy decreased after doping the  $\text{Tb}^{3+}$  ion. This result is strong agreement with that of **Table 1.2.3** (average bond distance of Ce-O). According to the equation between the crystal field and the bond length;  $Dq \propto 1 / R^5$  (where,  $Dq$  is crystal field strength, and  $R$  is bonding length between activators and anions) [62], the shorter average bond distance between  $\text{Ce}^{3+}$  and  $\text{O}^{2-}$  contributes to the increase of the crystal field around  $\text{Ce}^{3+}$  ion. Therefore,  $5d$  energy level of  $\text{Ce}^{3+}$  ion has larger split, and band gap energy was decreased ( $2.562 \text{ eV} \rightarrow 2.548 \text{ eV}$ ). As a result,  $(\text{Gd}_{0.79}\text{Ce}_{0.20}\text{Tb}_{0.01})_2\text{W}_2\text{O}_{9+\delta}$  pigment showed the highest  $b^*$  (+65.2) values and the smallest band gap energy ( $2.548 \text{ eV}$ ).

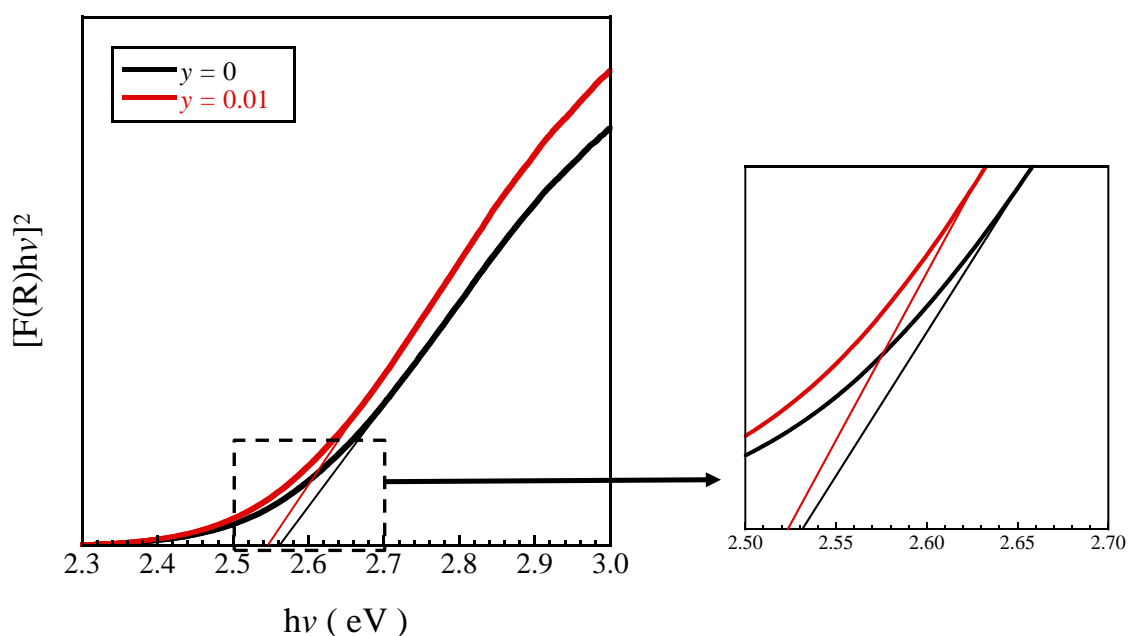


**Figure 1.2.11** Plots of  $[F(R)hv]^2$  against the photon energy ( $h\nu$ ) for indirect band gap deduction for  $(\text{Gd}_{0.80-y}\text{Ce}_{0.20}\text{Tb}_y)_2\text{W}_2\text{O}_{9+\delta}$  ( $y = 0$  and  $0.01$ ) pigments.

**Table 1.2.4** Color parameters and band gap energies for  $(\text{Gd}_{0.80-y}\text{Ce}_{0.20}\text{Tb}_y)_2\text{W}_2\text{O}_{9+\delta}$  ( $0 \leq y \leq 0.03$ ) pigments

| Samples   | $L^*$ | $a^*$ | $b^*$ | $C$  | $H^\circ$ | $E_g / \text{eV}$ |
|---|-------|-------|-------|------|-----------|-------------------|
| $(\text{Gd}_{0.80}\text{Ce}_{0.20})_2\text{W}_2\text{O}_{9+\delta}$                 | 78.5  | +11.5 | +63.5 | 65.7 | 79.9      | 2.562             |
| $(\text{Gd}_{0.79}\text{Ce}_{0.20}\text{Tb}_{0.01})_2\text{W}_2\text{O}_{9+\delta}$ | 77.2  | +12.4 | +65.2 | 66.4 | 79.2      | 2.548             |
| $(\text{Gd}_{0.79}\text{Ce}_{0.20}\text{Tb}_{0.02})_2\text{W}_2\text{O}_{9+\delta}$ | 77.6  | +12.1 | +64.7 | 65.8 | 79.4      | 2.553             |
| $(\text{Gd}_{0.77}\text{Ce}_{0.20}\text{Tb}_{0.03})_2\text{W}_2\text{O}_{9+\delta}$ | 78.2  | +11.9 | +64.0 | 65.1 | 79.5      | 2.558             |

### 1.2.4 Conclusion

$(\text{Gd}_{1-x}\text{Ce}_x\text{Tb}_y)_2\text{W}_2\text{O}_{9+\delta}$  ( $0 < x \leq 0.30$ ;  $0 \leq y \leq 0.03$ ) were successfully synthesized by the conventional solid state reaction method as novel environmentally friendly inorganic yellow pigments.  $\text{Ce}^{3+}$  and  $\text{Tb}^{3+}$  ions were substituted into the  $\text{Gd}^{3+}$  ion site in the  $\text{Gd}_2\text{W}_2\text{O}_9$  lattice to produce a brilliant yellow color. The yellow color originates from  $4f^1-5d^1$  transition of  $\text{Ce}^{3+}$  ion, and  $\text{Tb}^{3+}$  substitution caused change of the crystal field around  $\text{Ce}^{3+}$  ion. As a result,  $(\text{Gd}_{0.79}\text{Ce}_{0.20}\text{Tb}_{0.01})_2\text{W}_2\text{O}_{9+\delta}$  pigment showed the most vivid yellow hue among the prepared samples, with chromatic parameters of  $L^* = 77.2$ ,  $a^* = +12.4$ ,  $b^* = +65.2$ ,  $C = 66.4$ , and  $H^\circ = 79.2$ , respectively.

## Chapter 2

# Synthesis of Novel Inorganic Orange Pigment using Transition Metal Ion as a colorant (Ni<sup>2+</sup>)

### 2.1 Introduction

In this chapter, novel environmentally friendly orange pigment using transition metal ion (Ni<sup>2+</sup>) as a colorant is described. A barium nickel diphosphate (BaNiP<sub>2</sub>O<sub>7</sub>) was chosen as a base material because it is composed of non-toxic elements and abundant presence in earth-crust, and this base material included Ni<sup>2+</sup> ion expected to be a colorant for environmentally friendly inorganic orange pigment. The BaNiP<sub>2</sub>O<sub>7</sub> has triclinic structure having  $P\bar{1}$  space group. The transition metal ions have been widely used as colorant from the past due to their colorful color [19-33]. The transition metal ions have a strong optical absorption in the visible light region originated by *d-d* transition, because the *d* sub-shell of transition metal ion is partially filled. For example, Cu<sup>2+</sup>, Ni<sup>2+</sup>, and Mn<sup>3+/5+</sup> ions produced from blue to green color, from orange to red color, and from violet to blue color, respectively. That's why BaNiP<sub>2</sub>O<sub>7</sub> also exhibits orange color, but shows a low chroma parameter (*C*) expressing the color saturation due to the much lower redness (*a*\* = +22.9) as compared to yellowness (*b*\* = +48.5) because the orange color exists between red color and yellow color. As explained in **chapter 1**, the color of pigment can be controlled by two parameters. Concentration and crystal field around colorant and these two parameter are controllable by doping other ions.

In order to develop the inorganic orange pigment, the Ni<sup>2+</sup> ion in the BaNiP<sub>2</sub>O<sub>7</sub> lattice was partially replaced with Mn<sup>2+</sup> ion, which dose not affecting the color because it shows a strong optical absorption in the near-UV region. The position and absorptance of optical absorption band originated from Ni<sup>2+</sup> ion depends on the doped Mn<sup>2+</sup> ion content. Therefore,

the substituted  $\text{Mn}^{2+}$  ion was optimized to identify the relationship between the condition (crystal field and concentration) of colorant and optical absorption, and the color properties were estimated.

## 2.1 Experimental Procedure

The  $\text{Ba}(\text{Ni}_{1-x}\text{Mn}_x)\text{P}_2\text{O}_7$  ( $0 \leq x \leq 0.3$ ) samples were synthesized by the conventional solid state reaction method. The stoichiometric amounts of  $\text{BaCO}_3$ ,  $\text{NiO}$ ,  $\text{Mn}_2\text{O}_3$ , and  $\text{H}_9\text{N}_2\text{PO}_4$  powder were mixed by an agate mortar, being followed by mixing with a planetary ball milling apparatus (Pulverisette 7 premium line, FRITSCH GmbH) at 300 rpm for 3h. The homogeneous mixture was calcined twice at 600 °C for 6 h under atmospheric air, and then obtained powder was sintered three times at 900 °C for 6 h under atmospheric air. The sintered mixture was ground at the end of each calcination processing in the agate mortar.

The result of X-ray fluorescence spectroscopy (XRF; Rigaku, ZSX-100e), which expresses the samples composition, indicated the good agreement with the nominal stoichiometric composition. The samples were characterized by X-ray powder diffraction (XRD; SmartLab, Rigaku) using  $\text{Cu-K}\alpha$  radiation (40 kV and 30 mA) to identify the crystal structure. The lattice volume was calculated from the XRD peak angles. Rietveld refinement analysis was determined to clarify the crystallographic data of the samples by using the RIETAN-FP program [55]. The optical reflectance spectra were obtained using a UV-vis spectroscopy (UV-2600, Shimadzu) with barium sulfate as a reference. The color properties of the samples were decided in terms of the CIE  $L^*a^*b^*$  system with a colorimeter (CR-400, Konica-Minolta). In this system, the parameter  $L^*$  expresses the brightness (100) or darkness (0) in a neutral grey scale, and the parameters  $a^*$  [red (+) - green axis (-)] and  $b^*$  [yellow (+) - blue axis (-)] represent the color, respectively. The chroma parameter ( $C$ ) presenting the color saturation of the pigment was calculated by the formula ( $C = [(a^*)^2 + (b^*)^2]^{1/2}$ ). The parameter

$H^\circ$  (hue angle) which ranges from 0 to  $360^\circ$  was obtained according to the following equation,  $H^\circ = \tan^{-1}(b^*/a^*)$ ; ( $35 \leq H^\circ \leq 70^\circ$  is for orange color).

### 2.3 Results and Discussion

**Figure 2.1** shows the XRD patterns of the  $\text{Ba}(\text{Ni}_{1-x}\text{Mn}_x)\text{P}_2\text{O}_7$  ( $0 \leq x \leq 0.3$ ) samples. It was clear that a single phase of triclinic  $\text{BaNiP}_2\text{O}_7$  structure was obtained in the range of  $x \leq 0.2$ , whereas  $\text{BaMnO}_3$  peak appeared as an impurity for the sample with  $x = 0.3$ . **Figure 2.2** illustrates the  $\text{Mn}^{2+}$  ion content dependence of triclinic lattice volume for the  $\text{Ba}(\text{Ni}_{1-x}\text{Mn}_x)\text{P}_2\text{O}_7$  ( $0 \leq x \leq 0.3$ ) samples. The lattice volume of triclinic  $\text{BaNiP}_2\text{O}_7$  phase in the prepared samples was linearly increased with increasing  $x$  in the single-phase region ( $x \leq 0.2$ ), because the ionic radius of  $\text{Mn}^{2+}$  ion (0.066 nm for 4 coordination [48]) is larger than that of  $\text{Ni}^{2+}$  ion (0.055 nm for 4 coordination [48]). However, the lattice volume of the triclinic  $\text{BaNiP}_2\text{O}_7$  phase became constant in the two-phase mixture region ( $x > 0.2$ ), confirming that  $x = 0.2$  is the solid solubility limit for the single phase of the triclinic  $\text{BaNiP}_2\text{O}_7$  structure.

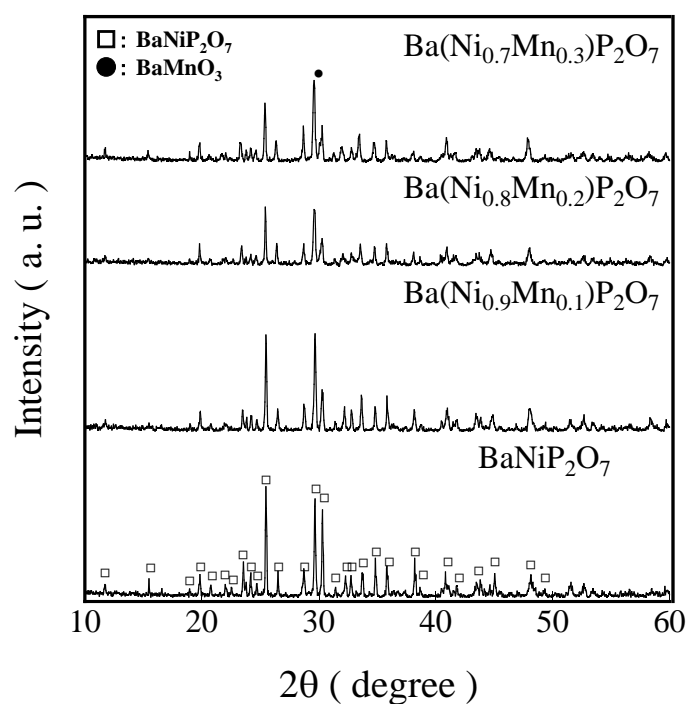


**Figure 2.1** XRD patterns of the  $\text{Ba}(\text{Ni}_{1-x}\text{Mn}_x)\text{P}_2\text{O}_7$  ( $0 \leq x \leq 0.3$ ) samples.

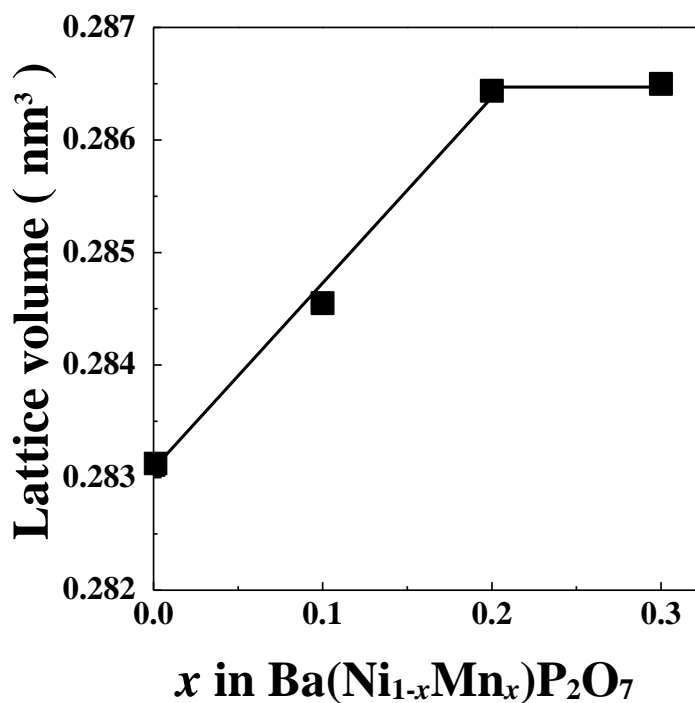


**Figure 2.2** Change in lattice volume for  $\text{Ba}(\text{Ni}_{1-x}\text{Mn}_x)\text{P}_2\text{O}_7$  ( $0 \leq x \leq 0.3$ ) samples as a function of  $x$ .

**Figure 2.3** illustrates the X-ray powder diffraction data obtained by Rietveld refinement for the  $\text{Ba}(\text{Ni}_{1-x}\text{Mn}_x)\text{P}_2\text{O}_7$  ( $0 \leq x \leq 0.2$ ) samples, and average bond distance of Ni-O for  $\text{Ni}_2\text{O}_8$  and  $\text{Ni}_2\text{O}_9$  units for the  $\text{Ba}(\text{Ni}_{1-x}\text{Mn}_x)\text{P}_2\text{O}_7$  ( $0 \leq x \leq 0.2$ ) samples are listed in **Table 2.1**. The Rietveld refinement results of  $\text{BaNiP}_2\text{O}_7$ ,  $\text{Ba}(\text{Ni}_{0.9}\text{Mn}_{0.1})\text{P}_2\text{O}_7$ , and  $\text{Ba}(\text{Ni}_{0.8}\text{Mn}_{0.2})\text{P}_2\text{O}_7$  samples showed the high reliability ( $R_{\text{wp}}$ ) values, which was 12.7, 11.8, and 10.8, respectively. The average bond distance of Ni-O for  $\text{Ni}_2\text{O}_8$  and  $\text{Ni}_2\text{O}_9$  units for  $\text{Ba}(\text{Ni}_{1-x}\text{Mn}_x)\text{P}_2\text{O}_7$  ( $0 \leq x \leq 0.3$ ) samples increased from 0.2132 nm to 0.2139 nm, and from 0.2230 nm to 0.2280 nm, respectively, with increasing  $\text{Mn}^{2+}$  ion content.

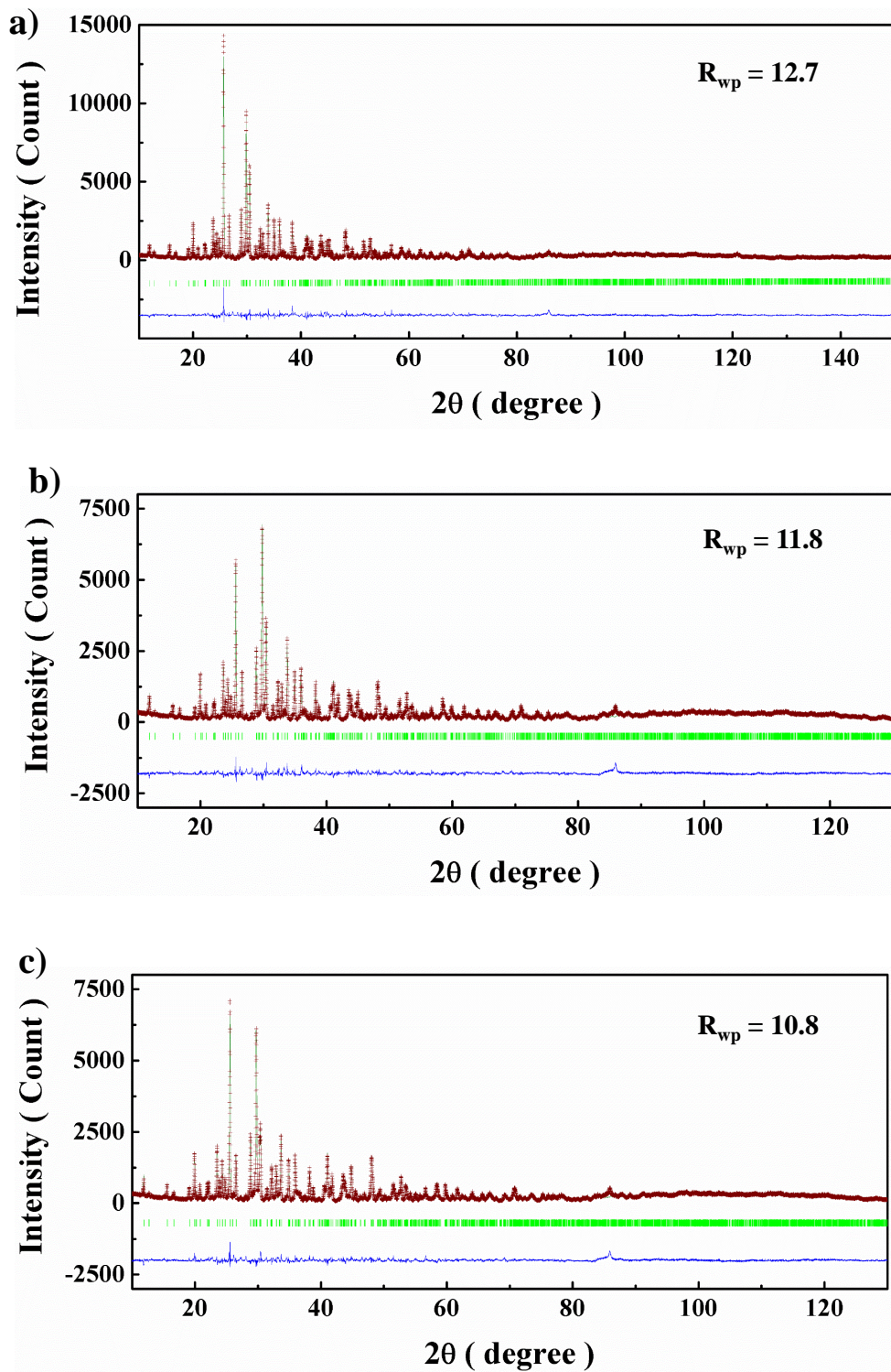


**Figure 2.3** Rietveld refinement results for the X-ray powder diffraction data for (a)  $\text{BaNiP}_2\text{O}_7$ , (b)  $\text{Ba}(\text{Ni}_{0.9}\text{Mn}_{0.1})\text{P}_2\text{O}_7$ , and (c)  $\text{Ba}(\text{Ni}_{0.8}\text{Mn}_{0.2})\text{P}_2\text{O}_7$  samples. Red symbol: measured pattern, green solid line: calculated pattern, blue solid line: difference between their intensities.

**Table 2.1** Average bond distance of Ni–O for BaNiP<sub>2</sub>O<sub>7</sub>, Ba(Ni<sub>0.9</sub>Mn<sub>0.1</sub>)P<sub>2</sub>O<sub>7</sub>, and Ba(Ni<sub>0.8</sub>Mn<sub>0.2</sub>)P<sub>2</sub>O<sub>7</sub> samples

| samples   | Ni–O average bond distance / nm |                                |
|---|---------------------------------|--------------------------------|
|   | Ni <sub>2</sub> O <sub>8</sub>  | Ni <sub>2</sub> O <sub>9</sub> |
| BaNiP <sub>2</sub> O <sub>7</sub>                                     | 0.2132                          | 0.2230                         |
| Ba(Ni <sub>0.9</sub> Mn <sub>0.1</sub> )P <sub>2</sub> O <sub>7</sub> | 0.2134                          | 0.2275                         |
| Ba(Ni <sub>0.8</sub> Mn <sub>0.2</sub> )P <sub>2</sub> O <sub>7</sub> | 0.2139                          | 0.2280                         |

The UV-vis diffuse absorption spectrum for the BaNiP<sub>2</sub>O<sub>7</sub> sample is depicted in **Figure 2.4**. The absorption spectrum for the BaNiP<sub>2</sub>O<sub>7</sub> sample was composed with several optical absorption bands originated from ligand-metal charge transfer (LMCT) and the *d-d* transition of Ni<sup>2+</sup>, which are composed with  ${}^3A_2({}^3F) \rightarrow {}^3T_1({}^3F)$ ,  ${}^3E({}^3F) \rightarrow {}^1A_1({}^1G)$ ,  ${}^3E({}^3F) \rightarrow {}^3E({}^3P)$ , and  ${}^3E({}^3F) \rightarrow {}^3A_2({}^3P)$ .

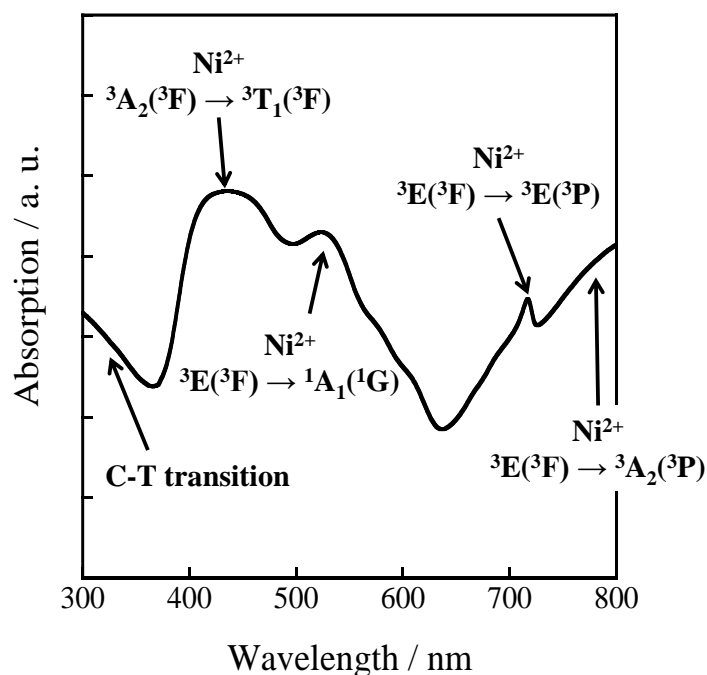


**Figure 2.4** UV-Vis diffuse absorption spectrum for BaNiP<sub>2</sub>O<sub>7</sub> sample.

The UV-vis diffuse reflectance spectra for the  $\text{Ba}(\text{Ni}_{1-x}\text{Mn}_x)\text{P}_2\text{O}_7$  ( $0 \leq x \leq 0.3$ ) samples are depicted in **Figure 2.5**, and the color parameters of the  $\text{Ba}(\text{Ni}_{1-x}\text{Mn}_x)\text{P}_2\text{O}_7$  ( $0 \leq x \leq 0.3$ ) samples are tabulated in **Table 2.2**. The reflectance for all samples in single-phase region increased with increasing  $\text{Mn}^{2+}$  ion content. It is due to a decrease of absorptance originated from  $d-d$  transition of  $\text{Ni}^{2+}$ , because the absorptance is proportional to concentration of colorant. Furthermore, the top position of reflectance in the range of 600 to 700 nm for all samples in the single-phase region was shifted to the red light region (longer wavelength direction) with increasing the  $\text{Mn}^{2+}$  ion content due to the decrease of crystal field around  $\text{Ni}^{2+}$  ion. As mentioned in **Chapter 1**, decrease of crystal field makes a smaller split for  $d-d$  energy level for  $\text{Ni}^{2+}$  ion, because the distance between colorant and anion is inversely proportional to crystal field and this phenomenon is exactly coincident with the result of Rietveld analysis. As a result,  $\text{Ba}(\text{Ni}_{0.8}\text{Mn}_{0.2})\text{P}_2\text{O}_7$  pigment showed the highest  $a^*$  (+28.6) value among the prepared samples.

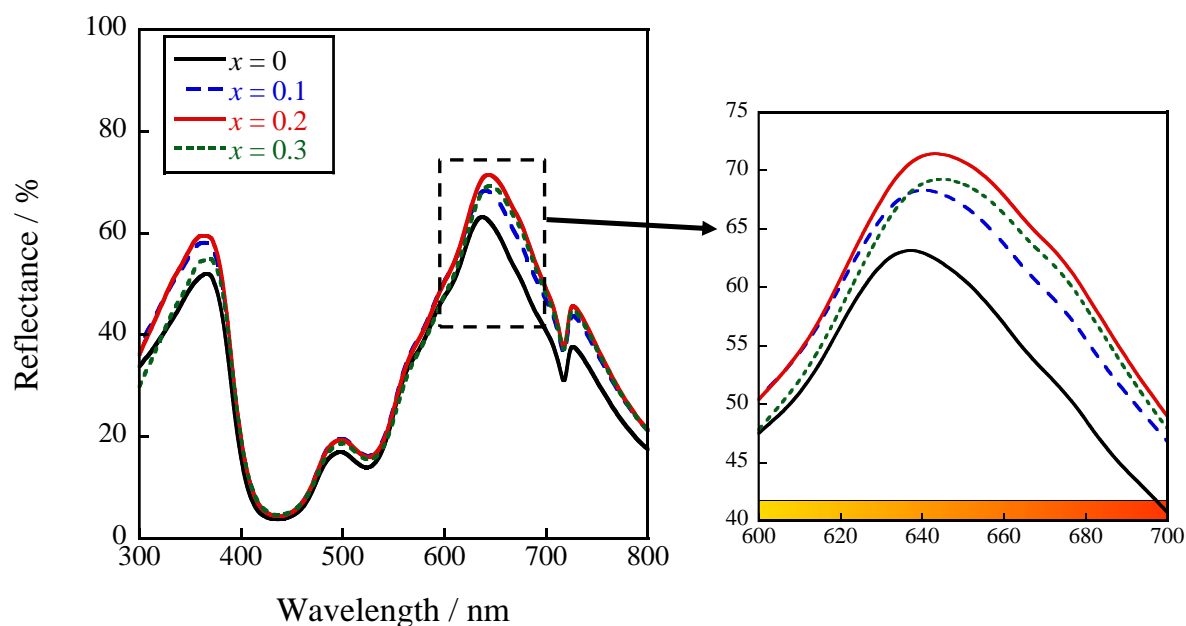


**Figure 2.5** UV-Vis diffuse reflectance spectra for  $\text{Ba}(\text{Ni}_{1-x}\text{Mn}_x)\text{P}_2\text{O}_7$  ( $0 \leq x \leq 0.3$ ) samples.

**Table 2.2** Color parameters for Ba(Ni<sub>1-x</sub>Mn<sub>x</sub>)P<sub>2</sub>O<sub>7</sub> (0 ≤ x ≤ 0.3) pigments

| Samples   | <i>L</i> * | <i>a</i> * | <i>b</i> * | <i>C</i> | <i>H</i> <sup>o</sup> |
|---|------------|------------|------------|----------|-----------------------|
| BaNiP <sub>2</sub> O <sub>7</sub>                                     | 66.9       | +22.9      | +48.5      | 53.6     | 64.7                  |
| Ba(Ni <sub>0.9</sub> Mn <sub>0.1</sub> )P <sub>2</sub> O <sub>7</sub> | 62.8       | +26.6      | +49.0      | 55.8     | 61.5                  |
| Ba(Ni <sub>0.8</sub> Mn <sub>0.2</sub> )P <sub>2</sub> O <sub>7</sub> | 59.6       | +28.6      | +46.8      | 54.8     | 58.6                  |
| Ba(Ni <sub>0.7</sub> Mn <sub>0.3</sub> )P <sub>2</sub> O <sub>7</sub> | 63.1       | +26.4      | +45.3      | 52.4     | 59.8                  |

## 2.4 Conclusion

Ba(Ni<sub>1-x</sub>Mn<sub>x</sub>)P<sub>2</sub>O<sub>7</sub> (0 ≤ x ≤ 0.3) were synthesized by the conventional solid state reaction method as novel environmentally friendly inorganic orange pigments. Mn<sup>2+</sup> ions were replaced into the Ni<sup>2+</sup> ion site in the BaNiP<sub>2</sub>O<sub>7</sub> lattice to further increase the red color. The red color was increased by control of the position and intensity of absorptance for Ni<sup>2+</sup> ion as colorant by optimizing the Mn<sup>2+</sup> ion content. Ba(Ni<sub>0.8</sub>Mn<sub>0.2</sub>)P<sub>2</sub>O<sub>7</sub> pigment showed the vivid orange color with the highest redness among the prepared samples, with chromatic parameters of *L*\* = 59.6, *a*\* = +28.6, *b*\* = +46.8, *C* = 54.8, and *H*<sup>o</sup> = 58.6, respectively.

## Chapter 3

# Synthesis of Novel Inorganic Orange Pigment with anisotropic structure and their high NIR reflectivity

### 3.1 Introduction

In this chapter, novel environmentally friendly orange pigment by control of anisotropic lattice distortion is described. Tetrastrontium dimanganese copper oxide ( $\text{Sr}_4\text{Mn}_2\text{CuO}_9$ ), which is composed with harmless elements, was focused on as a base material. The crystal structure of  $\text{Sr}_4\text{Mn}_2\text{CuO}_9$  with hexagonal perovskite 2H having the  $P321$  space group belongs to the  $\text{A}_{1+x}(\text{A}'_x\text{B}_{1-x})\text{O}_3$  ( $0 \leq x \leq \frac{1}{2}$ ) family. It has been reported that the conductivity of this structure was dramatically increased [63], and the magnetic and electronic properties of this structure caused from crystal anisotropic nature by another cation doping into the crystal lattice, which is strongly effected by the composition of A' and B sites in the lattice [63]. This unique feature of  $\text{Sr}_4\text{Mn}_2\text{CuO}_9$  can also possibly control the optical properties by doping another cation into A' and B sites in the lattice, although tetrastrontium dimanganese copper oxide shows the dark brown color.

In order to obtain the inorganic orange pigment by control of the anisotropic lattice distortion, the  $\text{Cu}^{2+}$  ion in the  $\text{Sr}_4\text{Mn}_2\text{CuO}_9$  lattice was partially or fully replaced with  $\text{Zn}^{2+}$  ion, which do not absorb in the visible light region because of its  $d^{10}$  configuration. As described above, the  $\text{Sr}_4\text{Mn}_2\text{CuO}_9$  sample ( $a^* = +13.7$ ,  $b^* = +23.8$ ) shows the dark brown color and has insufficient redness for an orange color pigment. The concentration of doped  $\text{Zn}^{2+}$  ion was optimized to improve the redness, and, furthermore, the relationship between optical properties and anisotropic lattice distortion was investigated.

## 3.2 Experimental Procedure

$\text{Sr}_4\text{Mn}_2(\text{Cu}_{1-x}\text{Zn}_x)\text{O}_9$  ( $0 \leq x \leq 1$ ) samples were synthesized by the conventional solid state reaction method.  $\text{SrCO}_3$  (99.99%, Wako Pure Chemical Industries),  $\text{Mn}_2\text{O}_3$  (99.9%, Mitsuwa Chemical),  $\text{CuO}$  (99.9%, Wako Pure Chemical Industries) and  $\text{ZnO}$  (99.9%, Wako Pure Chemical Industries) were mixed in a stoichiometric ratio using an agate mortar in which the concentration of Zn was in the range of 0 to 100 mol%. Then, a mixture was mechanically mixed by using a planetary ball milling apparatus (Pulverisette 7 premium line, FRITSCH GmbH) at 300 rpm for 3h. The homogeneous mixture was sintered at 1000 °C for 48 h in atmospheric air. Finally, the sintered powder was ground using a mortar.

The sample was identified by X-ray powder diffraction (XRD; SmartLab, Rigaku) with Cu-K $\alpha$  radiation (40 kV and 30 mA) to identify the crystal structure. The lattice volume was estimated from the XRD peak angles. The morphology and size of the synthesized particle were determined by scanning electron microscopy (SEM; Shimadzu, SS-550). The mean particle size and distribution were confirmed by measuring the diameter of 200 particles from SEM images. The optical reflectance spectra were measured using a UV-vis spectroscopy (UV-2600, Shimadzu) with barium sulfate as a reference and UV-vis-NIR spectroscopy (SolidSpec-3700, Shimadzu) with poly-tetrafluoroethylene (PTFE) as a reference. The color properties of the samples were estimated in terms of CIE  $L^*a^*b^*$  color system with a colorimeter (CR-400, Konica-Minolta). The parameter  $L^*$  indicates the brightness (100) or darkness (0) in a neutral grey scale, and the parameters  $a^*$  (the red-green axis) and  $b^*$  (the yellow-blue axis) represent the color, respectively. Chroma parameter ( $C$ ) expressing the color saturation of a pigment was calculated using the formula ( $C = [(a^*)^2 + (b^*)^2]^{1/2}$ ). Hue angle ( $H^\circ$ ) which ranges from 0 to 360° was calculated from the following equation,  $H^\circ = \tan^{-1}(b^*/a^*)$ ;  $H^\circ$  in the range 35° - 70° for orange color.

### 3.3 Results and Discussion

**Figure 3.1** depicts the XRD patterns of the  $\text{Sr}_4\text{Mn}_2(\text{Cu}_{1-x}\text{Zn}_x)\text{O}_9$  ( $0 \leq x \leq 1$ ) samples. X-ray powder diffraction (XRD) patterns of the  $\text{Sr}_4\text{Mn}_2(\text{Cu}_{1-x}\text{Zn}_x)\text{O}_9$  ( $0 \leq x \leq 1$ ) samples were in good agreement with single-phase of hexagonal structure. The lattice volumes calculated from the XRD peak angles of the  $\text{Sr}_4\text{Mn}_2(\text{Cu}_{1-x}\text{Zn}_x)\text{O}_9$  samples are plotted in **Figure 3.2**. The lattice volume increased with the increase in the  $\text{Zn}^{2+}$  ion content, which indicates the formation of solid solutions, because the ionic radius of  $\text{Zn}^{2+}$  (0.074 nm for 6 coordination [48]) is bigger than that of  $\text{Cu}^{2+}$  (0.073 nm for 6 coordination [48]). Where a solid solution is formed by introducing  $\text{Zn}^{2+}$  ion into  $\text{Cu}^{2+}$  ion site, the lattice volumes of  $\text{Sr}_4\text{Mn}_2(\text{Cu}_{1-x}\text{Zn}_x)\text{O}_9$  ( $0 \leq x \leq 1$ ) solid solution should vary linearly with increasing  $\text{Zn}^{2+}$  ion content because  $\text{Sr}_4\text{Mn}_2\text{CuO}_9$  and  $\text{Sr}_4\text{Mn}_2\text{ZnO}_9$  have same crystal structure (hexagonal) and space group (P 3 2 1(150)). However, the calculated lattice volumes of the  $\text{Sr}_4\text{Mn}_2(\text{Cu}_{1-x}\text{Zn}_x)\text{O}_9$  ( $0 < x < 1$ ) samples and the theoretical lattice volume change plotted as dot line were not exactly matched. This result implies the anisotropic lattice distortion of the  $\text{Sr}_4\text{Mn}_2(\text{Cu}_{1-x}\text{Zn}_x)\text{O}_9$  ( $0 < x < 1$ ), which had been reported to take the anisotropic crystal structure change accompanying the lattice volume variation by doping another cations [63].

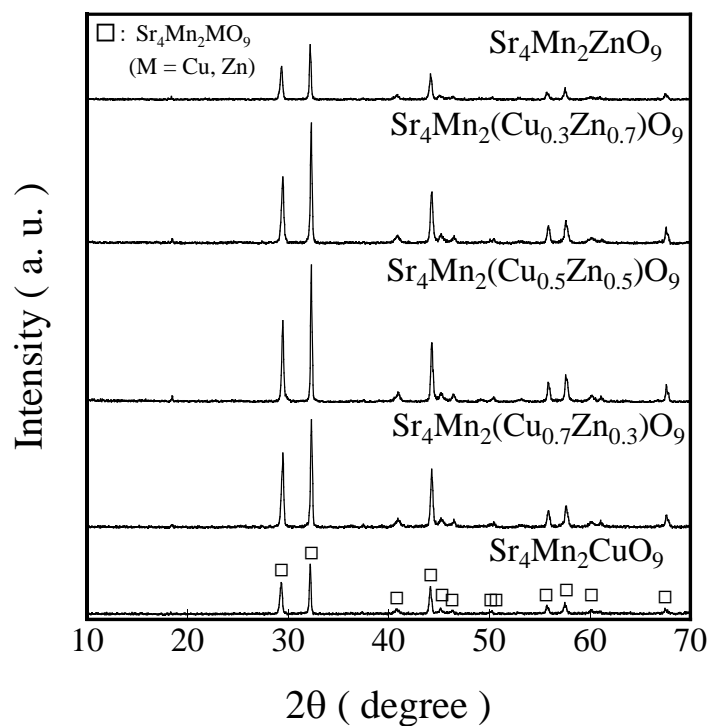


**Figure 3.1** XRD patterns of the  $\text{Sr}_4\text{Mn}_2(\text{Cu}_{1-x}\text{Zn}_x)\text{O}_9$  ( $0 \leq x \leq 1$ ) samples.

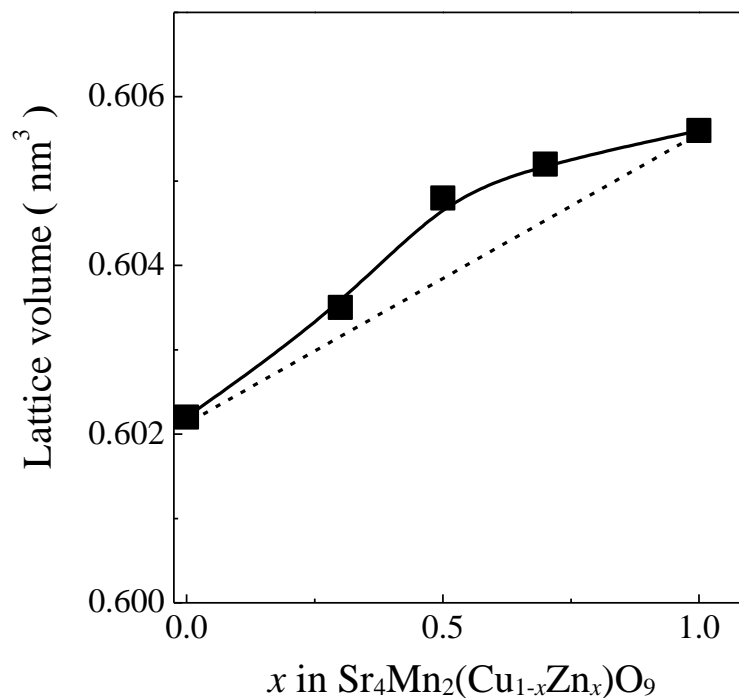


**Figure 3.2** Change in lattice volume for  $\text{Sr}_4\text{Mn}_2(\text{Cu}_{1-x}\text{Zn}_x)\text{O}_9$  ( $0 \leq x \leq 1$ ) samples as a function of  $x$ .

**Figure 3.3** indicates the XRD patterns of the  $\text{Sr}_4\text{Mn}_2(\text{Cu}_{1-x}\text{Zn}_x)\text{O}_9$  ( $0 \leq x \leq 1$ ) samples which were normalized based on the intensity of the (300) peak of the  $\text{Sr}_4\text{Mn}_2(\text{Cu}_{1-x}\text{Zn}_x)\text{O}_9$ . The peaks represented to the ( $lm0$ ), such as (300) or (330) peaks, displayed the same intensities for all samples. However, the peaks represented to the ( $lm2$ ), such as (112) and (222) for the  $\text{Sr}_4\text{Mn}_2(\text{Cu}_{1-x}\text{Zn}_x)\text{O}_9$  ( $0 < x < 1$ ) samples, showed the smaller intensity than those for  $\text{Sr}_4\text{Mn}_2\text{MO}_9$  ( $M = \text{Cu}$  and  $\text{Zn}$ ) samples, which are the end member of samples ( $x = 0, 1$ ). Furthermore, in the case of (222), the intensity of normalized XRD peak for the  $\text{Sr}_4\text{Mn}_2(\text{Cu}_{0.5}\text{Zn}_{0.5})\text{O}_9$  solid containing equal amount of  $\text{Cu}^{2+}$  and  $\text{Zn}^{2+}$  ions showed the smallest peak intensity among the prepared  $\text{Sr}_4\text{Mn}_2(\text{Cu}_{1-x}\text{Zn}_x)\text{O}_9$  ( $0 \leq x \leq 1$ ). This result also suggests that the lattice of the  $\text{Sr}_4\text{Mn}_2(\text{Cu}_{1-x}\text{Zn}_x)\text{O}_9$  ( $0 < x < 1$ ) samples containing both  $\text{Cu}^{2+}$  and  $\text{Zn}^{2+}$  ions in the crystal lattice is distorted, and it is coincident that shown in **Figure 3.2**.

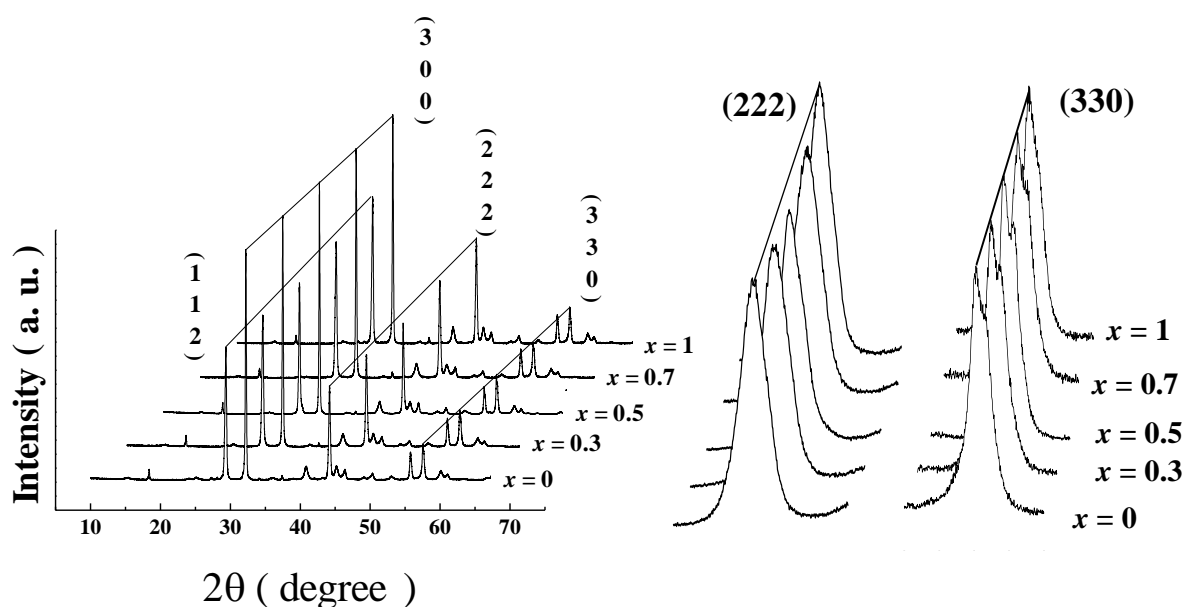


**Figure 3.3** Normalized XRD patterns for the  $\text{Sr}_4\text{Mn}_2(\text{Cu}_{1-x}\text{Zn}_x)\text{O}_9$  ( $0 \leq x \leq 1$ ) samples.

**Figure 3.4** illustrates the UV-Vis diffuse absorption spectra for the  $\text{Sr}_4\text{Mn}_2(\text{Cu}_{1-x}\text{Zn}_x)\text{O}_9$  ( $0 \leq x \leq 1$ ) samples.  $\text{Sr}_4\text{Mn}_2\text{MO}_9$  ( $\text{M} = \text{Cu}$  and  $\text{Zn}$ ) samples showed similar broad optical absorption bands although the intensity of optical absorption band is different. Divalent Zn ion having the  $d^{10}$  configuration does not show the  $d-d$  transition, although the materials containing transition metals are well known to have the broad optical absorption bands due to the  $d-d$  transitions of the transition metals. Therefore, similar optical absorption for  $\text{Sr}_4\text{Mn}_2\text{MO}_9$  ( $\text{M} = \text{Cu}$  and  $\text{Zn}$ ) samples indicates that the optical properties of the  $\text{Sr}_4\text{Mn}_2\text{CuO}_9$  sample does not affected by  $d-d$  transition of  $\text{Cu}^{2+}$  ion, and the optical absorption spectra for  $\text{Sr}_4\text{Mn}_2\text{MO}_9$  ( $\text{M} = \text{Cu}$  and  $\text{Zn}$ ) samples composed of the  $d-d$  transition of  $\text{Mn}^{4+}$  and ligand-metal charge transfer (LMCT) transition. The absorption spectra for the  $\text{Sr}_4\text{Mn}_2\text{MO}_9$  ( $\text{M} = \text{Cu}$  and  $\text{Zn}$ ) samples are composed with the several optical absorption bands originated from ligand-metal charge transfer (LMCT) transition and the  $d-d$  transition of  $\text{Mn}^{4+}$ . The broad optical absorption band at shorter wavelength than 450 nm is caused by the partial overlap of charge transfer (CT) transition and the  ${}^4\text{A}_2 \rightarrow {}^4\text{T}_1$  transition of  $\text{Mn}^{4+}$ . The absorption band centered at 500 nm represents to the  ${}^4\text{A}_2 \rightarrow {}^4\text{T}_2$  spin-allowed transition of  $\text{Mn}^{4+}$ . However, in the case of  $\text{Sr}_4\text{Mn}_2(\text{Cu}_{0.5}\text{Zn}_{0.5})\text{O}_9$  solid, the deformation of UV-vis diffuse reflectance profile was exhibited and can be explained by the anisotropic nature of crystal lattice. According to the results from XRD analysis and lattice volume, it was identified that the  $\text{Sr}_4\text{Mn}_2(\text{Cu}_{1-x}\text{Zn}_x)\text{O}_9$  ( $0 < x < 1$ ) samples have the anisotropic lattice distortion, and  $\text{Sr}_4\text{Mn}_2(\text{Cu}_{0.5}\text{Zn}_{0.5})\text{O}_9$  solid showed the largest anisotropy among the samples. As a result, the reflectance for the  $\text{Sr}_4\text{Mn}_2(\text{Cu}_{0.5}\text{Zn}_{0.5})\text{O}_9$  solid in the range of red light region (605 nm to 780 nm) increased due to the reduction of optical absorption related to the anisotropic lattice distortion, because the ligand-metal charge transfer (LMCT) transition is directly influenced by the crystal lattice.

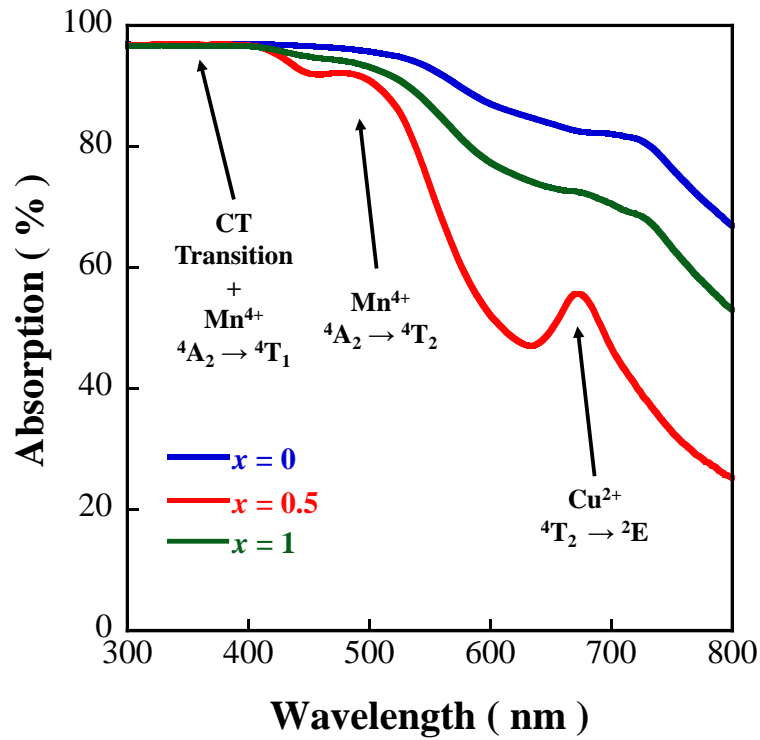


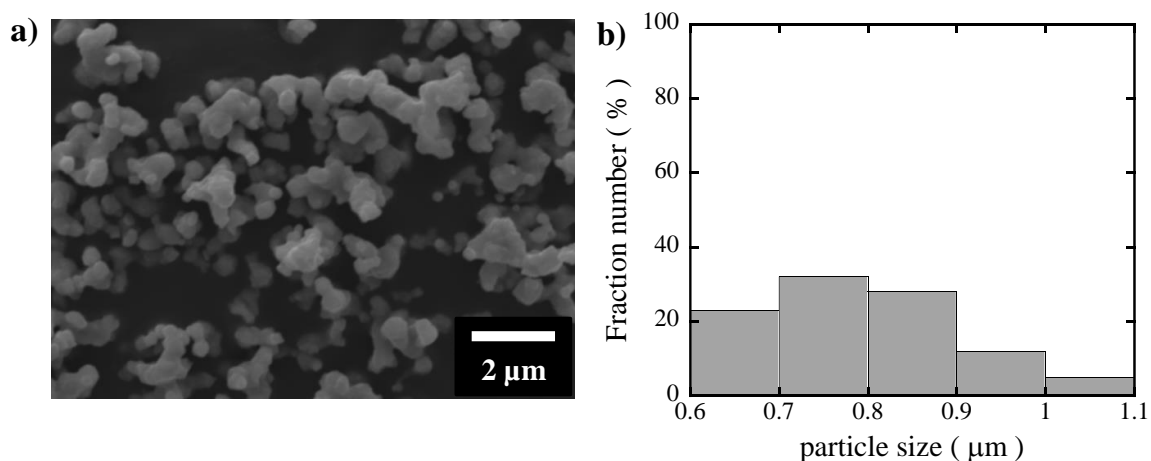
**Figure 3.4** Normalized XRD patterns for the  $\text{Sr}_4\text{Mn}_2(\text{Cu}_{1-x}\text{Zn}_x)\text{O}_9$  ( $0 \leq x \leq 1$ ) samples.

The color parameters of the  $\text{Sr}_4\text{Mn}_2(\text{Cu}_{1-x}\text{Zn}_x)\text{O}_9$  samples are listed in Table 3.1. As easily speculated from the result in **Figure 3.4**, the  $\text{Sr}_4\text{Mn}_2(\text{Cu}_{0.5}\text{Zn}_{0.5})\text{O}_9$  pigment showed the highest reflectance in the red light region (605 nm to 780 nm), as a result, this pigment exhibited the vivid orange color among the samples, whose color parameters were  $a^* = +19.8$ ,  $b^* = +52.3$ , and  $C = 55.9$  with the  $H^\circ = 69.3$ , because orange color is located between yellow color and red color.

**Table 3.1** Color parameters for the  $\text{Sr}_4\text{Mn}_2(\text{Cu}_{1-x}\text{Zn}_x)\text{O}_9$  ( $0 \leq x \leq 1$ ) samples

| Samples  | $L^*$ | $a^*$ | $b^*$ | $C$  | $H^\circ$ |
|--|-------|-------|-------|------|-----------|
| $\text{Sr}_4\text{Mn}_2\text{CuO}_9$                               | 37.2  | +13.7 | +23.8 | 27.5 | 60.1°     |
| $\text{Sr}_4\text{Mn}_2(\text{Cu}_{0.7}\text{Zn}_{0.3})\text{O}_9$ | 44.0  | +14.1 | +30.2 | 33.3 | 65.0°     |
| $\text{Sr}_4\text{Mn}_2(\text{Cu}_{0.5}\text{Zn}_{0.5})\text{O}_9$ | 64.0  | +19.8 | +52.3 | 55.9 | 69.3°     |
| $\text{Sr}_4\text{Mn}_2(\text{Cu}_{0.3}\text{Zn}_{0.7})\text{O}_9$ | 51.9  | +14.1 | +36.9 | 39.5 | 69.1°     |
| $\text{Sr}_4\text{Mn}_2\text{ZnO}_9$                               | 47.4  | +15.0 | +34.3 | 37.4 | 66.4°     |

The SEM image of the  $\text{Sr}_4\text{Mn}_2(\text{Cu}_{0.5}\text{Zn}_{0.5})\text{O}_9$  pigment synthesized in this study are shown in **Figure 3.5-a**). The mean particle size and size distribution of the pigment were estimated by measuring the diameters of 200 particles on the SEM photographs. The size distribution of these particles is illustrated in **Figure 3.5-b**). The  $\text{Sr}_4\text{Mn}_2(\text{Cu}_{0.5}\text{Zn}_{0.5})\text{O}_9$  pigment had a thermally diffused granular particle morphology due to the high calcination temperature (1000 °C), and the average particle size of the pigment was an approximately  $0.79 \pm 0.11 \mu\text{m}$ .

**Figure 3.5** (a) SEM image and (b) particle size distribution for the  $\text{Sr}_4\text{Mn}_2(\text{Cu}_{0.5}\text{Zn}_{0.5})\text{O}_9$  samples.

**Figure 3.6** shows the UV-vis-NIR reflectance spectra of the  $\text{Sr}_4\text{Mn}_2(\text{Cu}_{0.5}\text{Zn}_{0.5})\text{O}_9$  and bayferrox orange 960 pigments which is known as the commercially available orange pigment, and the value of the calculated NIR solar reflectance ( $R$ ) of these pigments are listed in **Table 3.2**. The NIR solar reflectance ( $R$ ) of the product was calculated as the integral of the measured spectral reflectance and the solar irradiance divided by the integral of the solar irradiance in the range of 700 to 2500 nm, as in the formula;

$$R = \frac{\int_{700}^{2500} r(\lambda) i(\lambda) d\lambda}{\int_{700}^{2500} i(\lambda) d\lambda}$$

where,  $r(\lambda)$  is the measured spectral reflectance ( $\text{Wm}^{-2}$ ) obtained from the UV-vis-NIR spectroscopy and  $i(\lambda)$  is the standard solar irradiance ( $\text{Wm}^{-2} \text{nm}^{-1}$ ) obtained from the American Society for Testing and Materials (ASTM) Standard G173-03 [64, 65]. The obtained NIR solar reflectance of the  $\text{Sr}_4\text{Mn}_2(\text{Cu}_{0.5}\text{Zn}_{0.5})\text{O}_9$  pigment was 83.03 %, which is remarkably higher than that of the commercially available bayferrox orange 960 pigment ( $R = 57.53$  %). This result signifies that the present  $\text{Sr}_4\text{Mn}_2(\text{Cu}_{0.5}\text{Zn}_{0.5})\text{O}_9$  orange pigment can be an energy saving material.

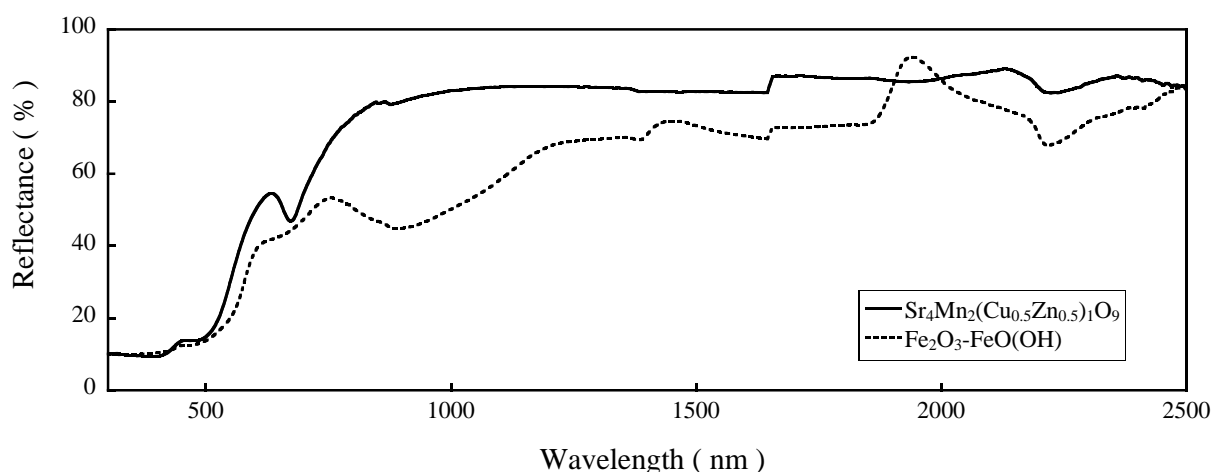


**Figure 3.6** UV-Vis-NIR reflectance spectra for the  $\text{Sr}_4\text{Mn}_2(\text{Cu}_{0.5}\text{Zn}_{0.5})\text{O}_9$  and bayferrox orange 960 ( $\text{Fe}_2\text{O}_3\text{-FeO(OH)}$ ) pigments.

### 3.4 Conclusion

$\text{Sr}_4\text{Mn}_2(\text{Cu}_{1-x}\text{Zn}_x)\text{O}_9$  ( $0 \leq x \leq 1$ ) were successfully synthesized by the conventional solid state reaction method as novel environmentally friendly inorganic orange pigments. It was confirmed that the anisotropic lattice distortion could be controlled by doping the  $\text{Zn}^{2+}$  ion. After  $\text{Zn}^{2+}$  ion doping, the  $\text{Sr}_4\text{Mn}_2(\text{Cu}_{0.5}\text{Zn}_{0.5})\text{O}_9$  pigment exhibited the vivid orange color, whose the chromatic parameters of  $L^* = 64.0$ ,  $a^* = +19.8$ ,  $b^* = +52.3$ ,  $C = 55.9$ , and  $H^\circ = 69.3$ , by the reducing of optical absorption in the red light region corresponding to the ligand-metal charge transfer (LMCT) transition owing to the anisotropic lattice expansion. Furthermore, the present  $\text{Sr}_4\text{Mn}_2(\text{Cu}_{0.5}\text{Zn}_{0.5})\text{O}_9$  pigment showed the superior NIR solar reflectance (83.03 %) which is remarkably higher than that (57.53 %) of the commercially available orange pigment ( $\text{Fe}_2\text{O}_3\text{-FeO(OH)}$ ). Therefore,  $\text{Sr}_4\text{Mn}_2(\text{Cu}_{0.5}\text{Zn}_{0.5})\text{O}_9$  pigment will be an effective alternative to the conventional one and also shows the potential as an energy saving material, since the present pigment consists of only harmless elements.

## Summary

In the work of this thesis, novel environmentally friendly inorganic pigments exhibiting a yellow, or orange colors have been successfully synthesized and their color properties were characterized. The obtained results through this study are summarized as follows:

### Chapter 1

- 1) Novel yellow pigments, the  $(\text{Ca}_{1-x-y}\text{Eu}_x\text{Zn}_y)_2\text{Al}_2\text{SiO}_{7+\delta}$  ( $0 < x \leq 0.15$ ;  $0 \leq y \leq 0.05$ ), were successfully synthesized by the conventional solid state reaction method. The color of these pigments depended on the concentration of  $\text{Eu}^{2+}$  ion as colorant, the proportion of  $\text{Eu}^{2+}$  ion increased by doping  $\text{Zn}^{2+}$  ion. Among the prepared pigments, the most vivid yellowness was obtained for  $(\text{Ca}_{0.87}\text{Eu}_{0.10}\text{Zn}_{0.03})_2\text{Al}_2\text{SiO}_{7+\delta}$  pigment, with a  $b^*$  value of +75.8.
- 2) Novel yellow pigments, the  $(\text{Ln}_{1-x}\text{Ce}_x)_2\text{W}_2\text{O}_{9+\delta}$  ( $\text{Ln} = \text{Pr}^{3+}$ ,  $\text{Sm}^{3+}$ , and  $\text{Gd}^{3+}$ ) and  $(\text{Gd}_{1-x}\text{Ce}_x\text{Tb}_y)_2\text{W}_2\text{O}_{9+\delta}$  ( $0 < x \leq 0.30$ ;  $0 \leq y \leq 0.03$ ) samples, were successfully prepared by the conventional solid state reaction method. The color of the pigments was strongly effected by the concentration and crystal field around of  $\text{Ce}^{3+}$  ion as colorant. Among the prepared pigments,  $(\text{Gd}_{0.79}\text{Ce}_{0.20}\text{Tb}_{0.01})_2\text{W}_2\text{O}_{9+\delta}$  pigment exhibited the most vivid yellowness, with a  $b^*$  value of +65.2.

### Chapter 2

Novel orange pigments,  $\text{Ba}(\text{Ni}_{1-x}\text{Mn}_x)\text{P}_2\text{O}_7$  ( $0 \leq x \leq 0.3$ ), were successfully obtained by the conventional solid state reaction method. The color of the pigments depended on the

intensity and position of the absorptance for Ni<sup>2+</sup> ion originated *d-d* transition. Among the prepared pigments, orange color with deepest red color ( $a^* = +28.6$ ) was obtained for Ba(Ni<sub>0.8</sub>Mn<sub>0.2</sub>)P<sub>2</sub>O<sub>7</sub> pigment.

### Chapter 3

Novel orange pigments, Sr<sub>4</sub>Mn<sub>2</sub>(Cu<sub>1-x</sub>Zn<sub>x</sub>)O<sub>9</sub> ( $0 \leq x \leq 1$ ) with hexagonal perovskite-type structure, were successfully developed by the conventional solid state reaction method. Orange color was realized from the reduction of absorptance in the red light region by doping Zn<sup>2+</sup> ions into the Cu<sup>2+</sup> ion sites in the Sr<sub>4</sub>Mn<sub>2</sub>CuO<sub>9</sub> lattice, and the color of the pigments was dependent on degree of anisotropic lattice distortion. Among the prepared pigments, the most vivid orange hue with deepest red color ( $a^* = +19.8$ ) was obtained for Sr<sub>4</sub>Mn<sub>2</sub>(Cu<sub>0.5</sub>Zn<sub>0.5</sub>)O<sub>9</sub> pigment, which contained both Cu<sup>2+</sup> and Zn<sup>2+</sup> ions in the crystal lattice. Furthermore, Sr<sub>4</sub>Mn<sub>2</sub>(Cu<sub>0.5</sub>Zn<sub>0.5</sub>)O<sub>9</sub> pigment showed the potential as an energy saving material due to their superior NIR solar reflectance (83.03 %), which is remarkably higher than that of commercial one.

## References

- [1] E. B. Faulkner, R. J. Schwartz, Weinheim, Wiley-VCH, 2009.
- [2] Rodgers, E Glen, New, McGraw-Hill College, 1994.
- [3] M. Onishi, Tokyo, Rikogakusha Publishing, 2000.
- [4] C. Gargori, S. Cerro, R. Galindo, A. García, M. Llusar, J. Badenes, G. Monrós, *Ceram. Int.*, 2011, **37**, 3665-3670.
- [5] V. Luz, M. Prades, H. Beltrán, E. Cordoncillo, *J. Eur. Ceram. Soc.*, 2013, **33**, 3359-3368.
- [6] Stewart R. 2 - EU legislation relating to electronic waste: the WEEE and RoHS Directives and the REACH regulations. Woodhead Publ Ser Electron Opt Mater 2012, 17–52.
- [7] P. Maestro, D. Huguenin, *J. Alloys Comp.*, 1995, **225**, 520–528.
- [8] G. Gauthier, S. Jobic, M. Evain, H. J. Koo, M. H. Whangbo, C. Fouassier, R. Brec, *Chem. Mater.*, 2003, **15**, 828–837.
- [9] M. Jansen, H.P. Letschert, *Nature*, 2000, **404**, 980–982.
- [10] N. Diot, O. Larcher, R. Marchand, J.Y. Kempf, P. Macaudière, *J. Alloys Comp.*, 2001, **323**, 45–48.
- [11] Q. Gao, X. Wu, Y. Ma, D. Li, Y. Fan, C. Du, *Ceram. Int.*, 2016, **42**, 17148–17153.
- [12] A. Han, Y. Zhou, M. Ye, S. Feng, H. Du, R. Yang, *Dye. Pigment.*, 2015, **123**, 242–247.
- [13] A. K. V. Raj, P. Prabhakar Rao, S. Sameera, S. Divya, *Dye. Pigment.*, 2015, **122**, 116–125.
- [14] D. Schildhammer, G. Fuhrmann, L. Petschnig, N. Weinberger, H. Schottenberger, H. Huppertz, *Dye. Pigment.*, 2017, **138**, 90–99.
- [15] T. Tsukimori, R. Oka, T. Masui, *Dye. Pigment.*, 2017, **139**, 808–811.
- [16] D. Schildhammer, G. Fuhrmann, L. Petschnig, H. Schottenberger, H. Huppertz, *Dye.*

- Pigment.*, 2017, **140**, 22–28.
- [17] S. Ke, Y. Wang, Z. Pan, *Dye. Pigment.*, 2014, **108**, 98–105.
- [18] G. George, V. S. Vishnu, M. L. P. Reddy, *Dye. Pigment.*, 2011, **88**, 109–115.
- [19] G. Buvaneswari, V. Aswathy, R. Rajakumari, *Dye. Pigment.*, 2015, **123**, 413–419.
- [20] R. Baitahe, N. Vittayakorn, S. Maensiri, *RSC Adv.*, 2015, **5**, 88890–88899.
- [21] Y. Shi, M. Zhong, Z. Zhang, D. Wang, *Ceram. Int.*, 2017, **43**, 5979–5983.
- [22] S. W. Kim, Y. Saito, T. Hasegawa, K. Toda, K. Uematsu, M. Sato, *Dye. Pigment.*, 2017, **136**, 243–247.
- [23] J. Li, S. Lorget, J. K. Stalick, A. W. Sleight, M. A. Subramanian, *Inorg. Chem.*, 2016, **55**, 9798–9804.
- [24] S. Tamilarasan, S. Laha, S. Natarajan, J. Gopalakrishnan, *J. Mater. Chem. C*, 2015, **3**, 4794–4800.
- [25] T. G. Kim, S. J. Kim, C. C. Lin, R. S. Liu, T. S. Chan, S. J. Im, *J. Mater. Chem. C*, 2013, **1**, 5843–5848.
- [26] D. Saraswathy, P. P. Rao, S. Sameera, V. James, A. K. V. Raj, *RSC Adv.*, 2015, **5**, 27278–27281.
- [27] V. James, P. Prabhakar Rao, S. Sameera, S. Divya, *Ceram. Int.*, 2014, **40**, 2229–2235.
- [28] P. Jiang, J. Li, A. W. Sleight, M. A. Subramanian, *Inorg. Chem.*, 2011, **50**, 5858–5860.
- [29] R. Oka, T. Masui, *RSC Adv.*, 2016, **6**, 90952–90957.
- [30] M. A. Pogosova, D. I. Provotorov, A. A. Eliseev, M. Jansen, P. E. Kazin, *Dye. Pigment.*, 2015, **113**, 96–101.
- [31] A. E. Smith, A. W. Sleight, M. A. Subramanian, *Mater. Res. Bull.*, 2011, **46**, 1–5.
- [32] J. Li, A. E. Smith, P. Jiang, J. K. Stalick, A. W. Sleight, M. A. Subramanian, *Inorg. Chem.*, 2015, **54**, 837–844.
- [33] S. Tamilarasan, D. Sarma, M. L. P. Reddy, S. Natarajan, J. Gopalakrishnan, *RSC Adv.*,

- 2013, **3**, 3199–3202.
- [34] T. Masui, H. Tategaki, N. Imanaka, *J. Mater. Sci.*, 2004, **39**, 4909–4911.
- [35] T. Masui, S. Furukawa, N. Imanaka, *Chem. Lett.*, 2005, **34**, 1322–1323.
- [36] T. Masui, S. Furukawa, N. Imanaka, *Chem. Lett.*, 2006, **35**, 1032–1033.
- [37] S. Furukawa, T. Masui, N. Imanaka, *J. Alloys Comp.*, 2008, **451**, 640–643.
- [38] N. Imanaka, T. Masui, S. Furukawa, *Chem. Lett.*, 2008, **37**, 104–105.
- [39] T. Masui, A. Shiraishi, S. Furukawa, Wendusu, N. Nunotani, N. Imanaka, *J. Jpn. Soc. Colour Mater.*, 2012, **85**[1], 9–13.
- [40] Wendusu, D. Kato, T. Masui, N. Imanaka, *Bull. Chem. Soc. Jpn.*, 2013, **86**, 283–288.
- [41] T. Masui, T. Honda, Wendusu, N. Imanaka, *Dye. Pigment.*, 2013, **99**, 636–641.
- [42] Wendusu, T. Honda, T. Masui, N. Imanaka, *Chem. Lett.*, 2013, **42**, 1562–1564.
- [43] Wendusu, T. Masui, N. Imanaka, *J. Asian Ceram. Soc.*, 2014, **2**, 195–198.
- [44] T. Masui, N. Takeuchi, H. Nakado, N. Imanaka, *Dyes Pigm.*, 2015, **113**, 336–340.
- [45] Q. Zhang, J. Wang, M. Zhang, Q. Su, *Appl. Phys. B*, 2008, **92**, 195–198.
- [46] P. Yang, X. Yu, H. Yu, T. Jiang, D. Zhou, J. Qiu, *J. Rare Earths*, 2012, **30**, 1208–1212.
- [47] G. A. Kumar, D. X. Liu, Y. Tian, M. G. Brik, D. K. Sardar, *Opt. Mater.*, 2015, **50**, 199–203.
- [48] R. D. Shannon, *Acta Crystallogr., Sect. A*, 1976, **32**, 751–767.
- [49] T. Maruyama, S. Morishima, H. Bang, K. Akimoto, Y. Nanishi, *J. Cryst. Growth*, 2002, **239**, 1167–1171.
- [50] L. A. Zavala-Sanchez, G. A. Hirata, E. Novitskaya, K. Karandikar, M. Herrera, O. A. Graeve, *ACS Biomater. Sci. Eng.*, 2015, **1**, 1306–1313.
- [51] D. Oliveira, A. L. M. Ferreira, J. M. Silva, M. R. Braga, G. S. Soledade, L. E. Aldeiza, *Dye. Pigment.*, 2008, **77**(1), 210–216.
- [52] S. Furukawa, T. Masui, N. Imanaka, *J. Alloys Comp.*, 2006, **418**, 255–258.

- [53] N. Diot, O. Larcher, R. Marchand, J. Kempf, P. Macaudie`re, *J. Alloys Comp.*, 2001, **323**, 45–48.
- [54] X. Qin, X. Liu, Huang, M. Bettinelli, X. Liu. *Chem. Rev.*, 2017, **117**, 4488–4527.
- [55] F. Izumi, K. Momma, *Solid State Phenom.*, 2007, **130**, 15–20.
- [56] K. Momma, F. Izumi, *J. Appl. Cryst.*, 2008, **41**, 653–8.
- [57] D. R. Eppler, R. A. Eppler, *Ceram. Eng. Sci. Proc.*, 1996, **17**, 77–87.
- [58] M. Kato, M. Takahashi, *J. Mater. Sci. Lett.*, 2001, **20**, 413–414.
- [59] B. Bae, S. Tamura, N. Imanaka. *Ceram. Int.*, 2017, **43(9)**, 7366–7368.
- [60] M. Romeo, K. Bak, J. Elfallah, F. Lenormand, L. Hilaire, *Surf. Int. Anal.*, 1993, **20**, 508–512.
- [61] E. Bêche, P. Charvin, D. Perarnau, S. Abanades, G. Flamant, *Surf. Int. Anal.*, 2008, **40**, 264–267.
- [62] K. Han, M. E. Hannah, A. Piquette, J. B. Talbot, K. C. Mishra, and J. McKittrick, *ECS J. Solid State Sci. Technol.*, 2012, 1, 98-102.
- [63] S. Aygün, S. Shiley, D. P. Cann, *Mater. Lett.*, 2004, **58**, 3645–3647.
- [64] Y. Zhang, Y. Zhang, X. Zhao, Y. Zhang, *Dyes Pigm.*, 2016, **131**, 154–159.
- [65] A. K. V. Raj, P. P. Rao, S. Sameera, S. Divya, *Dyes Pigm.*, 2015, 122, 116–125.

## Acknowledgements

The author would like to express his heartfelt gratitude to Professor Dr. Nobuhito Imanaka, Department of Applied Chemistry, Graduate School of Engineering, Osaka University, for his continuous guidance, many invaluable suggestions, and his science encouragement throughout the work. The author is indebted to Dr. Shinji Tamura, Department of Applied Chemistry, Graduate School of Engineering, Osaka University, for his continuous guidance and stimulating discussions for carrying out this work. The author is also very grateful to Dr. Naoyosi Nunotani, Department of Applied Chemistry, Graduate School of Engineering, Osaka University, for his helpful suggestions and apposite advice.

The author is deeply grateful to Professor Dr. Susumu Kuwabata, Department of Applied Chemistry, Graduate School of Engineering, Osaka University, and Professor Dr. Takahiro Kozawa, The institute of Scientific and Industrial Research (Department of Applied Chemistry, Graduate School of Engineering), Osaka University, for reviewing this thesis and giving their valuable comments.

Special thanks should be given to author's co-workers, Mr. Yuji hironaka and Mr. Akihiro Miura for their helpful assistance and support in the course of this work, and members of the research group under direction of Professor Dr. Nobuhito Imanaka, Osaka University. Whenever the author asked for help, they always meet my requirement without any hesitations.

The author would like to thank to Professor Dr. Dong Sik Bae, Department of Metallurgy and Materials Engineering, Changwon National University in South Korea, and Dr. In-Huck Song, Engineering Ceramics Department, Korea Institute of Materials Science (KIMS) in South Korea for his helpful comments and encouragement.

Finally, the author would like to deeply thank to his parents Mr. Gi Han Bae and Mrs.

Myoung Sook Son, his parents-in-law Mr. Su Gwan Lee and Mrs. Dong Suk Kang, his younger brother Mr. Byoung Wook Bae, his wife Mrs. Ju Eun Lee, and all the members of his family for their encouragement, continuous understanding, and perpetual supports.